Dalton Transactions

ROYAL SOCIETY OF CHEMISTRY

PERSPECTIVE

View Article Online
View Journal

Cite this: DOI: 10.1039/d0dt02143a

The role of photoinduced charge transfer for photocatalysis, photoelectrocatalysis and luminescence sensing in metal–organic frameworks

Xinlin Li, Sreehari Surendran Rajasree, Jierui Yu and Pravas Deria *

Received 16th June 2020,
Accepted 29th July 2020

DOI: 10.1039/d0dt02143a

rsc.li/dalton

Metal–organic frameworks (MOFs) have emerged as promising porous optoelectronic compositions for energy conversion and sensing applications. The enormous structural possibilities, the large variety of photo- and redox-active building blocks along with several post-synthetic functionalization strategies make MOFs an ideal platform for photochemical and photoelectrochemical developments. Because MOFs assemble all the active building units in a dense fashion, the non-aggregated yet proximally positioned species ensure efficient photon absorption to drive photoinduced charge transfer (PCT) reactions for energy conversion and sensing. Hence, understanding the PCT processes within MOFs as a function of the topological and electronic structures of the donor–acceptor (D–A) moieties can provide transformative strategies to design new low-density compositions.

I. Introduction

Metal–organic frameworks (MOFs) are an emerging class of porous compositions with modular topology and pore structure defining their desired properties.[1–5] These frameworks are commonly constructed by interconnecting metal-ion based secondary building units (SBUs) or nodes through organic linkers or struts, and the resulting porous compositions were originally projected as next-generation materials for separation and storage.[6–11] Over the years, these framework compositions have shown promising applications in photovoltaics,[12–14] photocatalysis,[15–21] and fluorescent sensors depending on the electronic properties of the components.[22–27] The enormous structural diversity, the molecular-scale porosity (for reactant/analyte delivery and product release), and the comparative ease of integration with redox-catalysts have made MOFs an attractive platform for photophysical and photochemical developments. The reticular framework chemistry has shown that linkers with similar molecular backbone can be assembled in identical topological networks, thus allowing the route for electronic tuning. Besides the flexible choices of linkers, MOFs can be post-synthetically functionalized[28–30] *via*, for example,

Department of Chemistry and Biochemistry, Southern Illinois University, 1245 Lincoln Drive, Carbondale, Illinois 62901, USA. E-mail: pderia@siu.edu

Xinlin Li

Xinlin Li obtained his B.S. in Chemistry (2014) and M.E. in Chemical Engineering (2017) from Lanzhou University, China. He is currently a Ph. D. student at Southern Illinois University, Carbondale, under the supervision of Prof. Pravas Deria. His current research focuses on the electrochemical and photophysical properties of various classes of metal-organic frameworks.

Sreehari Surendran Rajasree

Sreehari Surendran Rajasree obtained his integrated BS-MS in Chemistry (2019) from the Indian Institute of Science Education and Research Trivandrum, India. He joined Southern Illinois University, Carbondale, in the fall of 2019 for his graduate studies under the supervision of Prof. Pravas Deria. His current research focuses on improving light-harvesting in metal-organic frameworks.

linker modification,[28,31] metal or linker exchange,[32,33] or solvent-assisted ligand incorporation (SALI)[34–36] to integrate complementary functional chromophores or redox moieties with appropriate electronic properties and energies for the desired photoinduced processes. MOFs can be prepared both as crystalline and as amorphous variants; however, the former is the most studied form due to its precise and periodic positioning of the building units, which makes the understanding of the structure–property correlation easier. The key feature of these 3D solid porous frameworks is their ability to densely assemble chromophoric linkers (in hundreds of millimolar) around the pores. This ensures high photon absorptivity and provides a way to circumvent the extant challenges stemming from various unproductive exciton recombination processes observed in common molecular aggregates. Thus, the dense arrangement of chromophores in MOFs can constitute a near-ideal system for photocatalysis. For photoelectrocatalysis, MOF-modified electrodes can provide a higher areal concentration of accessible surface-bound catalysts compared to a traditional monolayer-based assembly.[37]

A photocatalytic process commonly starts with exciting antenna molecules by photon absorption, then the other components are sensitized *via* an energy transfer (EnT) process, and finally, the energy is delivered to catalytic sites for charge separation to generate redox equivalents for chemical transformation. This cascade of processes is reminiscent of the natural light-harvesting complexes (LHC) in photosystem I and II (PS-I/II), where more antenna pigments are assembled than the special pairs; such a system can be achieved in supramolecular assemblies like MOFs. Alternatively, the initially generated excited sensitizers can directly involve in charge-separation processes with appropriate complementary units, where the resulting charges (or redox equivalents) can take part in catalysis or initiate a migration chain to be carried away for further utilization.[15,38] Such systems have essentially the one-to-one ratio of the antenna component to the charge separation unit and are a simplified molecular or supermolecular version developed for synthetic ease. Nevertheless, a good photocatalyst must have high light absorptivity producing long-lived excited states to transfer the energy into relevant sites for charge separation, and importantly, a slow charge recombination rate is required for the system to initiate charge migration and/or driving chemical transformations. Photoinduced charge transfer (PCT), involving chromophoric linkers and metal SBUs,[39] or post-synthetically incorporated redox species (such as chromophores,[40–43] complexes,[44–46] metallic clusters,[47–49] and semiconducting nanostructures[50]), may prolong the overall lifetime of excited states for their meaningful utilization in catalysis. Therefore, understanding PCT between different photo-responsive moieties within MOFs would give insights for the design of highly efficient MOF-based photocatalysts.

The assembly of photoactive components in MOFs also makes them excellent candidates for luminescence sensing, where the detection of various analytes is based on the "turn-off" or "turn-on" process triggered by the PCT event. The "turn-off" mechanism involves the binding of analytes at the light-responsive component to quench its fluorescence *via* PCT between the excited fluorophore and the analyte. Such a quenching mechanism is not always accurate since other non-analyte factors may 'contaminate' the results by suppressing the fluorescence *via* undesired nonradiative decay. In contrast, the "turn-on" detection can be more accurate as it involves the specific analyte binding at one of the subunits of a donor (D)–acceptor (A) dyad to suppress the intra-molecular PCT and thereby facilitating a fluorescence recovery. This is commonly achieved by altering the electronic and/or energetics of the lowest unoccupied molecular/crystal orbital of the acceptor

Jierui Yu

Jierui Yu received his B.S. in Chemistry from Lanzhou University, China, in 2014. He is currently pursuing his doctoral studies in Southern Illinois University, Carbondale, under the guidance of Prof. Pravas Deria. His dissertation research is focused on the photophysical properties of metal-organic frameworks.

Pravas Deria

Dr. Pravas Deria earned a B.Sc. degree from the University of Calcutta and an M. Sc. from the Indian Institute of Technology Kanpur, India. He obtained his Ph.D. in Chemistry from the University of Pennsylvania, Philadelphia. After a fruitful postdoctoral tenure at Northwestern University, he joined the Department of Chemistry & Biochemistry at Southern Illinois University, Carbondale, as an assistant professor in 2015. His current research mainly focuses on the rational design of metal-organic frameworks and related porous coordination polymers for finding out unique photophysical, photochemical, and potentiometric properties for energy conversion applications.

subunit upon analyte binding (possibly by providing electron density from the analytes), which significantly inhibits the intramolecular electron transfer (ET) from donor to acceptor. The complete accessibility of such binding sites that are arranged in the proximity of photo-active components makes the MOF-based sensing system ideal and quick. These components, chosen based on their relative electronic properties, provide opportunities to tune the PCT within MOFs. Thus, understanding the underlying properties will guide the future development of MOF-based sensors.

Many contemporary works suggest that MOFs are emerging as optoelectronic compositions. Thus, photoinduced exciton generation and relevant harvesting *via* EnT, as well as transport of electrode-injected charges through redox hopping, are important steps; these phenomena have been diligently reviewed in several recent articles.[51–54] Given that PCT is another critical step in the same context, here we systematically discuss the excited-state properties of MOFs that drive photocatalysis, photoelectrocatalysis, and emission sensing. As such, screening MOF literature leads to many hits that report some kinds of photoinduced processes, where many interesting observations have been attributed to PCT in somewhat hand-waving fashion. Surprisingly, the proposed correlation of the underlying mechanism to a PCT is found to be made without the key spectroscopic data identifying the PCT intermediates. For this reason, we focus our discussion on the works that elaborate PCT with state-of-the-art spectroscopic techniques (*e.g.*, optical transient absorption (OTA/TA), electron paramagnetic resonance (EPR) spectroscopy, *etc.*) in MOF systems. We believe this understanding will shine a light on the future development of MOF photocatalysts and sensors.

II. Background of PCT

PCT processes may involve a transfer of a high energy electron from a photo-excited D to the LUMO of A, which can be described as follows:[55]

Step 1: excitation of D

$$D + A \rightarrow {}^{1,3}D^{*} + A$$

Step 2: delocalization of excited states in a D–A pair

$${}^{1,3}D^{*} + A \rightarrow {}^{1,3}(D - A)^{*}$$

Step 3: charge separation

$${}^{1,3}(D - A)^{*} \rightarrow {}^{1,3}(D^{\delta+} - A^{\delta-})^{*}$$

Step 4: formation of a radical ion pair

$${}^{1,3}(D^{\delta+} - A^{\delta-})^{*} \rightarrow {}^{1,3}(D^{\bullet+} - A^{\bullet-})^{*}$$

Step 5: formation of an electron transferred state

$${}^{1,3}(D^{\bullet+} - A^{\bullet-})^{*} \rightarrow D^{\bullet+} + A^{\bullet-}$$

(Singlet and triplet excited states are denoted by (1,3) in superscript).

Commonly, PCT starts with the vertical photoexcitation of D (Step 1). Electrons are excited from its highest occupied molecular orbital (HOMO) energy level to a higher energy level ($E_{ox}^{D\,*} = E_{ox}^{D} + E_{0,0}$). This excited-state can be delocalized over the D–A assembly (Step 2). In crystalline MOFs, the densely and precisely packed chromophores offer unique excited-state dynamics that can be fundamentally different from other assemblies like the stacked chromophore aggregates. The excited-states in MOFs can be delocalized over multiple chromophores defining molecular excitons that undergo a fast displacement *via* an efficient hopping process,[56,57] and drive ET with complementary chromophores or redox species with the appropriate alignment of frontier molecular/crystal orbitals.[58–60] However, the key feature that can be availed in MOFs is the tunable relative concentration of the complementary redox species. For those frameworks that assemble two types of linkers (*e.g.*, pillar-paddlewheel MOFs) or those where the ET pairs are constructed from linkers and metal SBUs, a long-distant EnT is not required. In contrast, for systems in which the complementary moieties are sparse, specifically those that are post-synthetically installed, an efficient EnT becomes a key step. The occurrence of ET (Step 3) will lead to the formation of a radical ion pair – the driving force of which would depend on the energy gap between the excited-state oxidation potential of the donor ($E_{ox}^{D\,*}$) and the ground-state reduction potential of the acceptor (*i.e.* when the ionization potential (I_{D^*}) of the excited D* is lower than the sum of the electron affinity of A and the Coulomb energy of the separated radicals). At each step, however, the excited species can recombine and relax back to the ground state both *via* radiative (emission of light) and non-radiative processes. Nevertheless, a useful strategy would be to prolong the lifetime of the charge-transferred states, which is commonly achieved by spatially displacing the charged species or changing the structure of the ET-complex by delocalization.[55]

An alternative case can be considered where the acceptor component is excited. In this scenario, with the LUMO (or LUCO, the lowest unoccupied crystal orbitals of MOFs) of D still being higher in energy relative to the excited-state oxidation potential of the acceptor ($E_{ox}^{A\,*}$), the hole-polaron in the excited acceptor is transferred to the donor at the ground state. This alternate process can be described from a perspective that depicts an electron being transferred from the donor (in the ground state) to the excited acceptor; this process involves the HOMO or HOCO (the highest occupied crystal orbital) of the relevant components. Thus, both processes are described through a generalized charge transfer (CT) probability that will involve the lowest unoccupied or highest occupied orbitals and be governed by their energetics and respective coupling terms.

Marcus theory has been widely used to analyze various CT reactions between inorganic redox couples in homogeneous systems,[61] electrochemical reactions on solid electrodes,[62,63] as well as biological[61] redox enzymes such as cytochromes,[64] peroxidase,[65,66] and photosynthetic enzymes.[67,68] The PCT processes among the redox entities in MOFs can also be analyzed

within the framework of Marcus theory,[61,69–72] in which the CT rate constant (k_{CT}) is expressed as the function of the free energy ΔG°:

$$k_{CT} = \frac{2\pi}{\hbar} {H_{DA}}^2 \frac{1}{\sqrt{4\pi\lambda_t k_b T}} \exp\left[-\frac{(\lambda_t + \Delta G^{\circ})^2}{4\pi\lambda_t k_b T}\right] \quad (1)$$

where H_{DA} represents the electronic coupling between the reactant and product, ΔG° is the thermodynamic driving force, and λ_t is the total reorganization energy. The term λ_t is the sum of internal reorganization energy (λ_i) and solvent oscillators (λ_s). The λ_i stems from the oscillators within the redox species and can be determined by the vibrational energy of all molecules in reactants (R) and products (P), whereas λ_s is calculated *via* the dielectric continuum model of the solvent. While the major factor defining the k_{CT} for a reaction is either H_{DA} or ΔG^{*} at a given temperature and has been well established over the last several decades, MOFs can provide unique opportunities to be exploited relative to those in molecular or hybrid homogeneous systems. This is because of the fixed and structure-dependent positioning of the D–A species defining $H_{DA} \propto e^{-\beta(r-r_0)}$, where r_0 is the contact distance between D and A, and β is the distance and dielectric dependent decay factor of the tunneling electron wave-functions. Microporous MOFs offer various features such as structural rigidity, a unique solvent orientation (relative to the bulk), and a micro/local environment; these can play critical roles in defining λ_t which may be difficult to achieve in a homogeneous macromolecular system and can only be observed in an elegant biological design.

Fig. 1a depicts the potential energy diagram of reactants and products as a function of nuclear coordinate in an endergonic reaction. A CT process can occur at the intersection of the potential energy surfaces where an overlap of the wavefunctions of R and P reaches a maximum. The activation energy ΔG^{*} required to pass this intersection is mathematically related to ΔG°:

$$\Delta G^{*} = (\lambda_t + \Delta G^{\circ})^2 / 4\lambda_t \quad (2)$$

Eqn (2) explains a quadratic relation of the rate with the driving force – the highest rate observed when the driving force becomes the same as the reorganization energy. Since a CT is too fast to allow the nuclei of R and P to shift their positions,[61] the electronic coupling element H_{DA} is distance-dependent and a strong coupling will enhance the CT probability in an adiabatic fashion (Fig. 1c). ΔG° can be calculated by using the Rehm–Weller eqn (3);[73,74] these values are often used to guide the design for the feasibility of PCT between the D and A species.

$$\Delta G^{\circ}_{CT} = e(E^{D}_{ox} - E^{A}_{red}) - \Delta E_{0,0} - \Delta G^{\circ}(\varepsilon) \quad (3)$$

Here, E^{D}_{ox} and E^{A}_{red} represent the ground state oxidation and reduction potential of D and A respectively; $E_{0,0}$ is the first excited-state energy of D. $\Delta G^{\circ}(\varepsilon)$ is the dielectric correction term based on the Born eqn (4):[74]

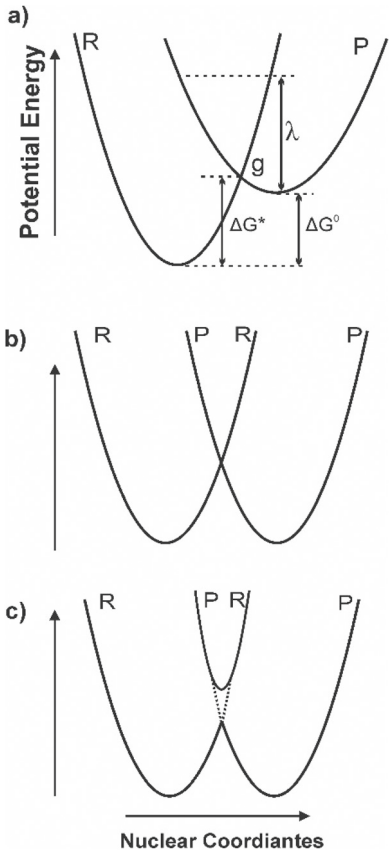

Fig. 1 (a) Potential energy diagrams of reactant (*R*) and product (*P*) for the endergonic reaction. Potential energy surface for the R and P in (b) nonadiabatic ET with insignificant and (c) adiabatic with strong electronic coupling (H_{DA}).

$$\Delta G^{\circ}(\varepsilon) = \frac{e^2}{4\pi\varepsilon_0\varepsilon_S R_{DA}} + \frac{e^2}{8\pi\varepsilon_0}\left(\frac{1}{r_D} - \frac{1}{r_A}\right)\left(\frac{1}{\varepsilon_{ref}} - \frac{1}{\varepsilon_S}\right) \quad (4)$$

where ε_0 is the permittivity of free space, ε_s is the static dielectric constant of the solvent, and ε_{ref} is the dielectric constant of the solvent where the redox potentials were measured. The first term of eqn (4) reflects the interaction energy between the DA radical ions with radii r_D and r_A at a center to center distance R_{DA}, where the second term corrects the difference of ion solvation between a solvent of interest and solvent where the redox potential was measured.

III. PCT in MOFs

PCT in MOFs begins with photonic energy absorption by either chromophoric linkers, metal SBUs, or both. Here, the CT can occur within the intrinsic structural components of the framework (*e.g.* a linker, metallic building blocks); alternatively, a guest component that was installed or infiltrated into the framework can be involved. PCT in MOFs can involve

either a linker-to-metal (LMCT), linker-to-linker (LLCT), or host–guest components as long as it satisfies the requirements: (i) the relative energetics of the frontier orbitals of the D–A pair are properly aligned to drive a CT in an energetically favorable manner; (ii) the center-to-center distance of the D–A dyad lies within the range of the exciton delocalization radius of D. We will discuss the PCT in MOFs within the intrinsic components and installed/infiltrated system.

III.A. PCT between intrinsic structural components as a donor–acceptor pair

PCT between intrinsic structural components would either require MOFs with one type of linker and redox-active metal node with appropriate coordination geometry defining its potential energy and ligand-field transitions or two redox-active linkers (with inactive metal ions (*e.g.* Zn^{II}, Zr^{IV}, *etc.*) based node) as seen in pillar-paddlewheel type structures. Recently, the intrinsic LMCT between linkers and metal building blocks within the framework has been extensively studied using spectroscopy. The Huang group has explored the excited states and CT dynamics within a cobalt zeolitic imidazolate framework known as ZIF-67 (Fig. 2a) using various steady-state and transient spectroscopic techniques such as ultraviolet-visible (UV-Vis), femto-nanosecond (optical) transient absorption (fs/ns-OTA), and X-ray transient absorption (XTA) spectroscopy.[39] Fig. 2c shows the UV-Vis-near IR absorption spectrum of a ZIF-67 film. The characteristic absorptions at 300, 590, and 900–1400 nm (broad) are attributed to an LMCT, and higher-energy [$^4A_2(F) \rightarrow {}^4T_1(P)$] and lower-energy [$^4A_2(F) \rightarrow {}^4T_1(F)$] ligand field transitions as depicted in Fig. 2b. The fs-OTA spectra recorded by exciting the MOF sample at 1000 nm (*i.e.* [$^4A_2(F) \rightarrow {}^4T_1(F)$] transition) highlight several key processes when probed in the visible region (475–700 nm). These include a ground state bleach (GSB) due to a depletion of $^4A_2(F)$ population (Fig. 2d; at 520–600 nm) and a weak broad transient absorption at 640–700 nm for the excitation of the populated $^4T_1(F)$ state (Fig. 2d inset). The excited $^4T_1(F)$ state decays to form a long-lived intermediate state (IMS) that can be seen by the rise of the absorption band centered at 525 nm and 605 nm. The excited-state dynamics were globally analyzed with the bi-exponential fitting of the fs-OTA (Fig. 2e) and the ns-OTA kinetic data, probed at 580 and 608 nm, respectively. From these fittings, the authors determined a fast 31.7 ps component attributed to the IMS formation and two longer, 0.64 and 9.2 μs, components as the lifetime of the IMS (a weighted average lifetime of 2.9 us). The authors probed the dynamics of the higher $^4T_1(P)$ state by selectively exciting the sample with a 530 nm pump (compared to a 1000 nm light that preferably excites $^4T_1(F)$ from the $^4A_2(F)$ ground state). A similar global analysis of the kinetic data reveals two additional time-constants: a 0.45 ps lifetime attributed to the $^4T_1(P) \rightarrow {}^4T_1(F)$ relaxation and a new 0.95 ps component assigned to the direct IMS formation (*i.e.*, $^4T_1(P) \rightarrow$ IMS). A similarity between the OTA spectra of the IMS state and the second derivative of the GSB led the authors to postulate that the observed IMS state is a long-lived charge-separated (CS) state. To prove this hypothesis, the authors recorded XANES spectra (Fig. 2f) before (*i.e.* under a 'laser-off' condition) and after 527 nm excitation (*i.e.* a 'laser-on' -excited condition), which showed a broad positive transient absorption between 7714.9 and 7725.3 eV where 1s–4p shake-down[75] and 1s–4p transition[76] occur. This characteristic signature indicates a red-shifted transition, *i.e.* the edge of the cobalt-center shifts to a lower energy, possibly due to the photoreduction of Co^{II} *via* LMCT. This long-lived charge-separated state shows the potential of ZIF-67 in photocatalysis in energy conversion processes.

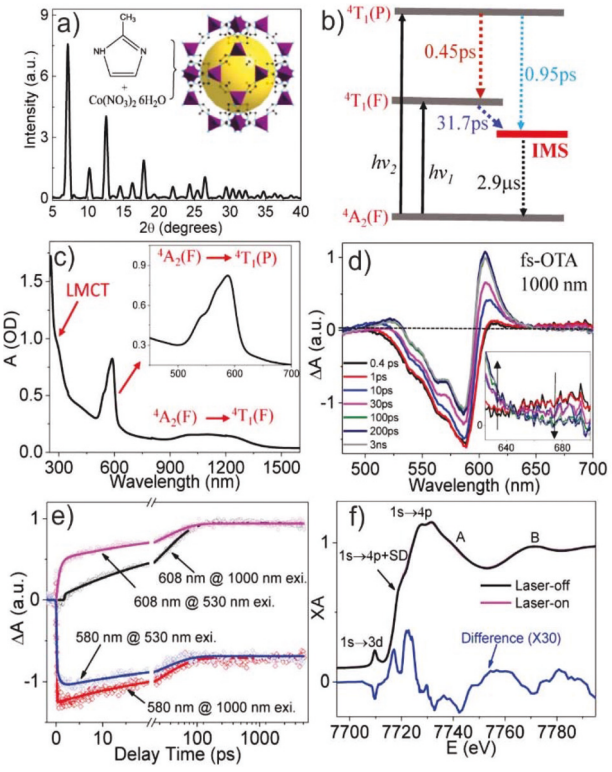

Fig. 2 (a) Chemical structure and powder XRD patterns of ZIF-67; (b) the schematic representation of the energy diagram of Co^{2+} (T_d) and excited state relaxation processes in ZIF-67; (c) UV-Vis-Near IR absorption spectrum of ZIF-67; (d) fs-OTA spectra of ZIF-67 at 1000 nm; (e) kinetics at 608 nm and 580 nm in fs-OTA spectra of ZIF-67 after 1000 nm and 530 nm excitation. (f) XANES spectrum of ZIF-67 at the Co K-edge before (laser-off) and 500 ps after laser excitation (laser on). Reproduced with permission from ref. 39. Copyright 2016, American Chemical Society.

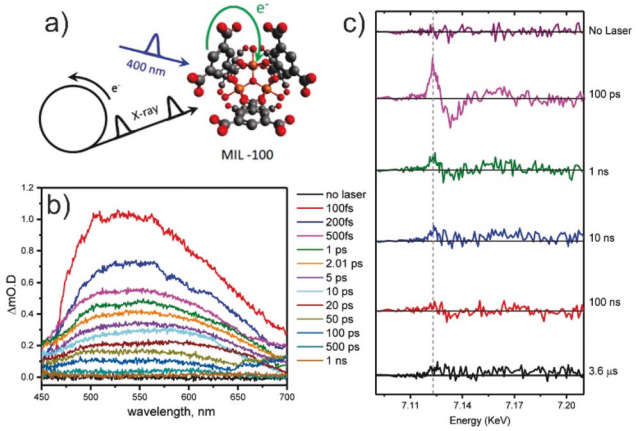

Fig. 3 (a) Schematic illustration of LMET from the excited linker to Fe_3-μ_3-oxo clusters; (b) OTA spectra collected at different time delays (λ_{ex} = 400 nm); (c) XTA difference spectra obtained at multiple time delays for MIL100(Fe) Reproduced with permission from ref. 77. Copyright 2017, American Chemical Society.

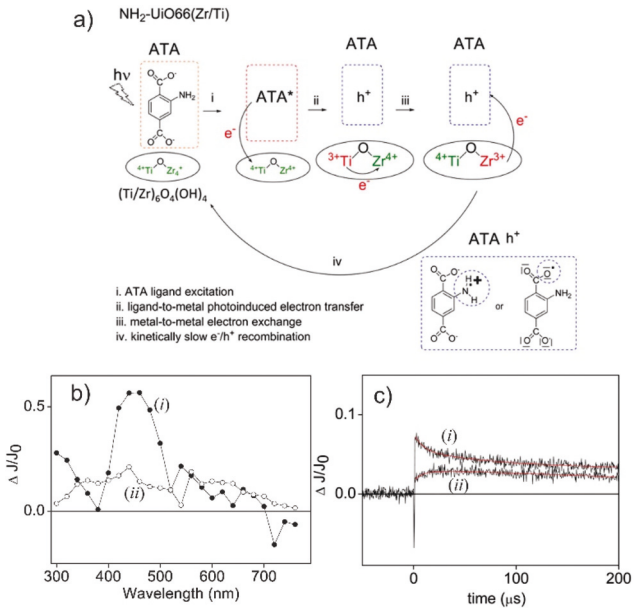

Fig. 4 (a) Scheme depicting the Ti^{3+}–O–Zr^{4+} species as a mediator for LMET in NH_2-UiO-66(Zr/Ti); (b) UV-vis diffuse reflectance TA spectra recorded (i) 3 and (ii) 184 μs after 355 nm laser pulse under nitrogen atmosphere for NH_2-UiO-66(Zr/Ti-35%). (c) Kinetic profile monitored at (i) 450 and (ii) 540 nm after 355 nm laser pulse under nitrogen atmosphere for NH_2-UiO-66(Zr/Ti-35%). Reproduced with permission from ref. 81. Copyright 2017, American Chemical Society.

signal observed up to 3.6 μs delay time confirms the long-lived CT excited state, which could be stabilized by electron delocalization within the Fe_3-μ_3-oxo clusters, which can be a good strategy to achieve a useful long-lived PCT state.

Titanium dioxide has been explored as a promising photocatalyst due to a low-lying Ti^{IV}–Ti^{III} valence exchange band featuring a UV responsive bandgap. This unique electronic property has made this material a good photoanode layer in dye-sensitized solar cells. This has triggered an extensive investigation into the band structure of titanium oxide-based MOFs for a possible PCT involving organic linkers.[78–80] In one such study, Portillo *et al.* prepared amino-UiO-66 derivatives denoted as NH_2-UiO-66(Zr/Ti). These hybrid porous compositions were constructed from deprotonated 2-aminoterephthalic acid (ATA), with exchanged Ti species up to 35% onto the Zr-oxo nodes, and were investigated for the role of Ti-doped Zr-oxo clusters in PCT.[81] The diffuse reflectance TA spectra (Fig. 4b) of NH_2-UiO-66(Zr/Ti-35%) displayed two absorption bands at 450 and 540 nm recorded at 3 and 184 μs delay times after the 355 nm laser pulse (samples with lower Ti doping have similar analogous spectra). The fitting of kinetic profiles (Fig. 4c) monitored at 450 nm featured two lifetimes τ_1 = 8.6 ± 2.3 μs (45%) and τ_2 > 200 μs (55%), whereas the 540 nm profile has a rising (single) component with τ_{rising} = 8.5 ± 2.5 μs. The 450 nm TA band was assigned as the excited-state transition in the triplet manifold of NH_2-UiO-66(Zr/Ti), which displays a faster decay profile mediated by molecular oxygen. With the similarity between the time constant for the fast decay component measured at 450 nm absorption (*i.e.* τ_1 = 8.6 ± 2.3 μs) and the rising lifetime of the 540 nm band (τ_{rising} = 8.5 ± 2.5 μs), the authors inferred that the formation of the transient species associated with the 540 nm absorption commences (~40%) from the decay of the triplet state. The 540 nm absorption is assigned to the conversion of Ti^{4+} to Ti^{3+}, verified by an analogous homogeneous quenching experiment between ATA and Ti^{4+}. Based on these TA results, it was proposed that LMCT can occur from an ATA* to the $(Ti/Zr)_6O_4(OH)_4$ node forming Ti^{3+}–O–Zr^{4+} species that can live long enough to possibly drive chemical transformation. This result can be compared to an analogous experiment by Gascon and co-workers who reported that the pristine NH_2-UiO-66(Zr) MOF (*i.e.* without any Ti-dopant) does not facilitate any LMCT process. This is due to a larger band gap for the Zr-oxo cluster, which is aligned in a way that does not facilitate electronic interaction with the organic linker. Therefore, the photoexcitation leads to a linker-centered, short-lived excited-state within the pristine NH_2-UiO-66(Zr) MOF.[82]

On the other hand, the electronic and redox properties of linkers can also be a key factor for modulating the LMCT to Ti-oxo clusters. Padial *et al.* reported a hydroxamate-based MOF MUV-11 constructed by reacting benzene-1,4-dihydroxamic acid (H_4bdha) with titanium(IV) isopropoxide in dimethylformamide (DMF). The chelating moiety in this linker is different from the typical carboxylates. Computational modeling revealed that a hydroxamate siderophore binder causes a drastic change of the frontier orbitals in the MOF, thereby suppressing the CT kinetics (*i.e.* less likely to undergo LMCT from the hydroxamate linker to Ti clusters).[83] In common titanium-carboxylate based MOFs, such as Ti-terephthalate (*i.e.* MIL-125-NH_2 with a chemical formula $Ti_8O_8(OH)_4$(bdc-NH_2)$_6$, where bdc is 1,4-benzenedicarboxylate), it has been established that photoexcitation will lead to LMCT generating photo-reduced Ti^{III} which can be probed by EPR spectra.[84] The

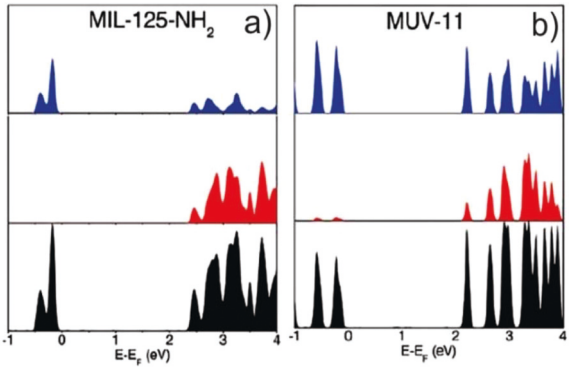

Fig. 5 Total (black) and projected (Ti in red and ligand in blue) density of states for (a) MIL-125-NH_2, (b) MUV-11. Reproduced with permission from ref. 83. Copyright 2019, American Chemical Society.

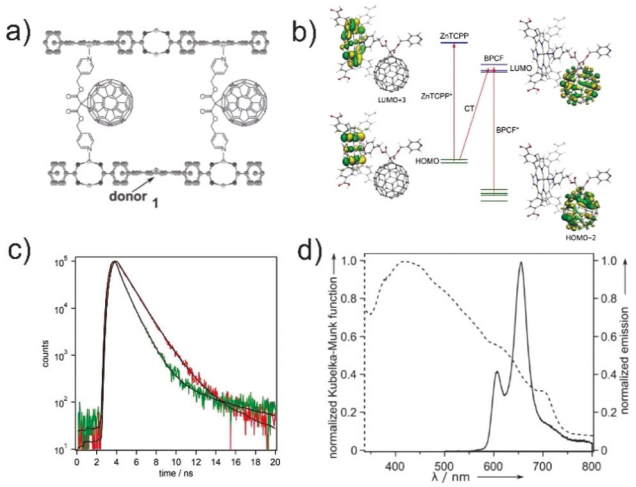

Fig. 6 (a) Structure of a porphyrin-fullerene pillar-paddlewheel MOF where BPCF serves as both an energy and electron-accepting linker in the crystalline framework; (b) computationally obtained energy diagram and molecular orbitals of the C_{60}–ZnTCPP molecular dyad. The red arrows show three types of excitation anticipated in this system; (c) transient fluorescence decays of C_{60}@PMOF (green) and Zn_2(ZnTCPP) (red); (d) normalized diffuse reflectance of BPCF (dashed line) and emission of the two-dimensional porphyrin-based framework Zn2-(ZnTCPP) (solid line). Reproduced with permission from ref. 86. Copyright 2016, Wiley-VCH.

electronic density of states (DOS; Fig. 5a) shows that for the carboxylate MOFs, the HOCO is localized at the organic linker, whereas the LUCO is titanium-node centered. Such frontier orbital alignments provide a thermodynamically favorable driving force with a negative LMCT energy. In contrast, the Ti-hydroxamate MOF – *i.e.* the MUV-11 exhibits a linker-centered LUCO (Fig. 5b) with a high orbital contribution of *ca.* 70%. The electronic structure indicates a linker localized excited-state in MUV-11 with more or less no driving force for LMCT, which is consistent with the fact that photoexcitation did not produce any paramagnetic signal from the photoreduced Ti^{III} species (as opposed to the common Ti-carboxylate systems). As a result, MUV-11 did not display any photocatalytic HER activity. This study demonstrated that the electronic properties of metal SBUs and organic linkers (as function of the electronic properties of their side group functionality and the binding moiety) can significantly impact the PCT within frameworks, and therefore this fact should be considered while designing MOF-based catalytic systems.

Fullerenes and their derivatives are widely used as excellent electron acceptors in PCT processes,[85] especially in organic photovoltaics, where they aggregate and form electron transport media. Likewise, installing fullerene within MOF pores can serve two purposes: fullerene can act as a PCT component and an electron-transport channel, depending on the loading density. In one such assembly, the photophysical behavior of a fullerene-based MOF was investigated. The Shustova group prepared a multilayered pillar-paddlewheel crystalline framework containing a porphyrin-fullerene dyad as a D–A pair.[86] The MOF can be defined as slipped-layers of tetrakis(4-carboxyphenyl)porphyrinato zinc(II) (TCPPZn) formed through the zinc-carboxylate based paddle-wheel node, where the fullerene derivative, bis(pyridin-4-ylmethyl)-3′H-cyclopropa-[1,2](C_{60}-Ih)[5,6]fullerene-3′,3′-dicarboxylate (BPCF), served as the pillar binding two Zn centers, one of TCPPZn and the other from the node at the neighboring layer (Fig. 6a). The absorption of BPCF (A) and emission of ZnTCPP indicate a significant spectral overlap as the requirement of Förster resonance energy transfer (FRET) from D to A (Fig. 6d). Based on the fluorescence lifetime quenching (Fig. 6c) of ZnTCPP (*i.e.* from 1.07 to 0.54 ns), the energy-transfer efficiency and rate constant were estimated to be 49.5% and 9.18×10^8 s^{-1}, respectively. The Förster critical radius (R_o) was estimated as 18.8 Å by calculating the spectral overlap function ($J = 2.34 \times 10^{-15}$ cm^3 M^{-1}), which is longer than the D–A distance extracted from structural data. Besides FRET, the authors noted that PCT can also be responsible for the lifetime quenching of ZnTCPP. However, this presumption was only supported by time-dependent DFT calculations that showed that the charge-transfer excitation has a similar energy to that of C_{60}-based excitation (Fig. 6b) and no direct characteristic spectral evidence was presented. Thus, the thermodynamics of the FRET and CT processes is predicted to be comparable.

III.B. PCT between the non-framework complementary D–A pair

Given that crystalline MOFs can be used as a solid architectural platform, the available pores can be systematically utilized to host exogenous species other than the solvent. These complementary chromophores and/or redox-active species, in molecular form, can be installed at a precise location by, for example, making postsynthetic modifications of the side-chain functionality of linkers or at the node (other postsynthetic methods such as exchange and ligand incorporation can also be used, *vide infra*). Alternatively, a diffusive infiltration can be used to fill (pack) the pore with the complementary species.

III.B.1. Systems with postsynthetically installed/anchored components. Zirconium MOFs have become popular due to

their robust nature and electronic properties that are relevant for photophysical studies including PCT. Being a group-IV transition metal, Zr_6^{IV} -oxo node can be anticipated to have similar optoelectronic behavior to that of a Ti^{IV}-oxo derived node that frequently features an LMCT from excited organic linkers.[38] However, computational studies suggest that the conduction band of the zirconium-oxo node lies 2 eV wider than that of the benzenedicarboxylate linker due to the high energy of zirconium 4d orbitals.[87] Thus, a photo-induced LMCT from a common π-conjugated linker to the Zr_6^{IV}-oxo node is unlikely to occur unless the excited state oxidation potential of the linker is unusually high in energy. This electronic property of the Zr_6^{IV}-oxo nodes makes them unique in a way that the linker orbitals do not electronically interact with each other. As a result, the Zr_6^{IV}-oxo nodes become optoelectronically "inert" in the UV-vis region relative to most π-conjugated organic linkers. Hence, Zr_6^{IV}-oxo derived frameworks provide desired chemically and mechanically robust platforms where various photophysical studies including PCT can be examined among different linkers and other components as a function of their crystallographic position. The Zr^{IV}-ions may exert a 'heavy atom' effect facilitating singlet-to-triplet intersystem crossing processes, but no study has established this yet. Nevertheless, the chemical constituents of such metal-oxo node may play a key role in defining the CT kinetics.

Most Zr_6^{IV}-oxo MOFs can host a wide range of secondary organic or inorganic species, which further extend the possibilities of realizing donor–acceptor dyad systems. This is because, a majority of the Zr_6^{IV}-oxo MOFs possess large pores ranging from 10 Å to over 50 Å depending on the topological net.[88–93] These pores are suitable to incorporate complementary species including small organic species,[34,94] organometallic species,[95–99] clusters,[49,100–103] or even small enzymes.[104–106] Furthermore, common Zr_6^{IV}-oxo SBUs construct 12 or 8-carboxy connected MOFs: thus, an unsaturated 8-connected Zr_6-oxo node can be exploited to install carboxy-terminated redox species *via* a well-established process called solvent assisted linker incorporation (SALI).[34,95,107] Alternatively, a 12 connected MOF (*e.g.* UiO-66) with the variable extent of defects (*i.e.* missing linkers, capped with a monocarboxylate such as formate) can be defect-exchanged/engineered.[108–110] Both these postsynthesis processes are technically the same as they involve the replacement of non-framework ligands (like hydroxy and carboxy) with an incoming carboxylate or phosphonate.[111]

In this context, a well-known Zr_6^{IV}-oxo MOF NU-1000 has been used as a host platform. Here, an assembly of a deprotonated 1,3,6,8-tetrakis(p-benzoic acid)pyrene linker (TBAPy) acts as an antenna for photon harvest. A study reported by the Deria group showed that immobilizing carboxy-ferrocene (Fc) at the Zr-oxo node forming Fc@NU-1000 (Fig. 7a) quenches the MOF emission *via* a CT from the Fc to the photo-excited TBAPy (Fig. 7b).[95] It is important to note that less than one Fc per four TBAPy linkers is enough to reach the saturation quenching; this observation indicates another interesting feature in MOFs: an efficient EnT enhances the quenching per-

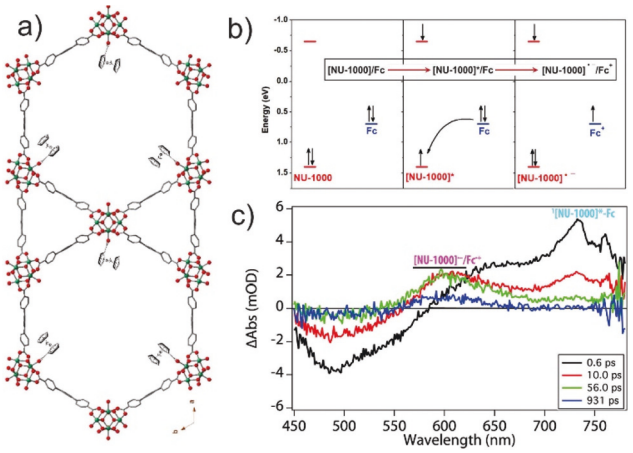

Fig. 7 (a) Structure of Fc@NU-1000; (b) energy diagram depicting the PET process from Fc to excited NU-1000 in Fc@NU-1000; (c) representative fs-TA spectra of Fc@NU-1000 under the excitation of 400nm. Reproduced with permission from ref. 95. Copyright 2018, American Chemical Society.

imeter of a redox quencher. The fs-TA spectroscopic data of Fc@NU-1000 highlight the instant appearance of an intense singlet ($S_1 \rightarrow S_n$) excited state absorption (ESA) at 730 nm (Fig. 7c; TA spectrum at 0.6 ps); this signature, which is reminiscent of that of excited pristine NU-1000, was assigned [NU-1000]*/Fc. The singlet excited population then quickly decays to a new ESA appearing at 600 nm and is assigned $[NU\text{-}1000]^{\bullet-}/Fc^{+}$. Given a close Fc-pyrene distance (*ca.* 10 Å), k_{CT} was determined (from the rise time of the 600 nm band) to be very efficient 7.4×10^{10} s^{-1} (τ_{CT} = 9 ps) with a relatively slow thermal charge recombination (τ_{CR} = 430 ps). Interestingly, solvent-dependent k_{CT} data determined from the emission quenching experiments (using time-resolved fluorescence data) revealed that the CT process is nonresponsive to dielectric modulation. This is because the node-bound Fc-moieties experience a polar microenvironment formed by the protruding hydroxyl/aqua ligands at the Zr_6^{IV}-oxo node. Thus, the CT process in Fc@NU-1000 involves a high 'solvent' reorganization energy (λ_0) to drive $[NU\text{-}1000]^{\bullet-}/Fc^{+}$ formation. A partial capping of the hydroxyl/aqua ligands was seen to slightly increase the rate.[38]

In an attempt to emulate the functionality of the chlorophyll based LHCs, Deria and coworkers showed that complementary pigment-assemblies within MOFs can be a viable way. For this, they first post-synthetically anchored a tetraphenylporphyrinato zinc(II) (TPPZn) derived complementary pigment within the 1D pores of NU-1000 MOF forming a D–A system.[107] This design is based on the appropriate alignment of the ground and excited-state redox potentials of donor and acceptor in a way that it facilitates an EnT from the excited MOF (*i.e.*, NU-1000*) to TPPZn forming TPPZn*. Here, the excited TBAPy linker assembly in the framework serves as the antenna to harvest photonic energy and efficiently deliver it to the adjacent TPPZn anchored on the Zr-oxo node *via* FRET

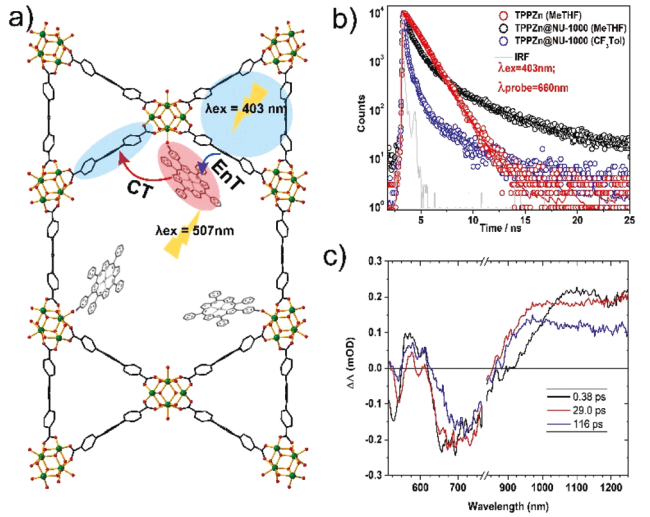

Fig. 8 (a) Scheme of photoinduced electron/energy transfer in a typical TPPZn@NU-1000 structure, depicting the energy and charge transfer between TPPZn and Pyrene under the excitation of 403 and 507nm. (b) Transient emission decay profiles of NU-1000, TPPZn, and TPPZn@NU-1000 in two solvents (λ_{ex} = 403 nm, λ_{probe} = 660 nm); (c) representative fs-TA spectra of Fc@NU-1000 under the excitation of 400nm. Reproduced with permission from ref. 107. Copyright 2019, American Chemical Society.

($k_{EnT} \approx 4.7 \times 10^{11}$ s^{-1}; τ_{EnT} = 2 ps; Fig. 8a).[107] Given that the excited-state oxidation potential of [TPPZn]* lies 0.54 eV higher than the ground-state reduction potential of NU-1000, a spontaneous CT was observed from [TPPZn]* to NU-1000. The process can be considered as the excited TPPZn pigment forming a special pair like the system with a neighboring TBAPy linker to drive the CT. The PCT was studied *via* transient emission that revealed a solvent polarity dependent rate: a $k_{CT} = 6.2 \times 10^8$ s^{-1} and 1.2×10^{10} s^{-1} (*i.e.* $\tau_{CT} \sim 1.6$ ns and 80 ps) in 2-methyltetrahydrofuran (MeTHF) and trifluorotoluene (CF_3Tol) solvents, respectively. This is an interesting finding for two reasons. First, the highest rate recorded for TPPZn@NU-1000 is about one order magnitude slower than what was observed for the Fc@NU-1000 system ($k_{CT} \approx 1 \times 10^{11}$ s^{-1}; $\tau_{CT} \sim 10$ ps) even though the Zn-pyrene distance (*ca.* 8.7 Å) is slightly shorter than the Fc-pyrene distance. This is possibly due to a negligible internal reorganization energy for the Fc-centered redox process in a way that the driving force ($\Delta G°$) matches with the total reorganization energy. Second, the TPPZn@NU-1000 composition displays a significant solvent polarity dependent rate: *ca.* 20-fold difference in k_{CT} going from the MeTHF to CF_3Tol solvent compared to a negligible solvent response in Fc@NU-1000. This is because TPPZn is fixed far from the polar Zr-oxo SBUs compared to the Fc-moiety: d_{Fe-Zr} = 5.6 Å in Fc@NU-1000, where d_{Zn-Zr} = 12.75 Å in TPPZn@NU-1000. The fs-TA spectroscopic data collected for TPPZn@NU-1000 (in the CF_3Tol solvent) clearly display an unambiguous signal for the GSB (540 nm) and $S_1 \rightarrow S_0$ stimulated emission (660 nm) of TPPZn*, where a broad NIR transient at 976 nm is evinced for $TPPZn^{\bullet+}$, and the signal for $[NU\text{-}1000]^{\bullet-}$ at ~600 nm is obscured by the TA signal of TPPZn* and its stimulated emission bands. However, the evolution of the red-shifted stimulated emission peak of TPPZn* (660 nm → 700 nm) attests to the underlying rise of $[NU\text{-}1000]^{\bullet-}$ (at ~600 nm; the blue side of the stimulated emission band) over time. The global fitting of the transient dynamical data probed at 541, 693, and 976 nm reveals a 283 ps charge recombination time constant. The design of this system also highlights an impressive spectral coverage of the system: the TPPZn moiety absorbs light energy complementary to the TBAPy assembly and can be excited directly through its low energy Q band derived transition (at 530 nm) and thus, the TPPZn@NU-1000 composition covers a large (350–650 nm) effective window of the solar spectrum and excitation at any wavelength within this entire range can lead to $TPPZn^{\bullet+}$/$[NU\text{-}1000]^{\bullet-}$ CT-state formation. Given that the PCT generated charge-carriers in TPPZn@NU-1000 (with a $\tau_{CR} \simeq 280$ ps) can migrate *via* redox hopping[112–114] through both TBAPy and the TPPZn units, respectively, they can be harvested in a photoelectrochemical setup (IPCE ≃ 0.36% at 532 nm, −0.5 V *vs.* Ag/AgCl).

III.B.2. Systems with postsynthetically infiltrated components. Depending on the size and shape of the pores, a post-synthetic infiltration process may differ. For example, in cage-like pores, one would have to introduce the secondary guest component during synthesis or employ a dynamic window opening facilitated by a linker exchange process. In this 'ship-in-a-bottle' scenario, the incorporated species is larger than the largest pore window and thus remains 'corked' inside with some limited conformational and rotational flexibility. For 1D pores, however, the complementary species can be diffused inside the pores with varying density. Here, the incorporated species can form a close-packed column or may establish a non-covalent interaction with the aromatic linker, albeit depending on the solvent. Although the latter process may not provide precise control of the position of the incorporated species, it is a simple method for the preparation of the bulk composition.

PCT processes resulting from triplet excited states have also been studied within host–guest systems in MOFs; the advantage here is a prolonged sensitizer lifetime enabling energy migration and/or driving relatively slower CT with a larger structural reorganization. Larsen and coworkers encapsulated the $[Ru(2,2'\text{-bipyridine})_3]^{2+}$ photosensitizer, commonly known as Rubpy, into a MOF in a ship-in-a-bottle fashion. Here, the CoRWLC-2 framework was constructed from a solvothermal reaction of 1,3,5-tris(4-carboxyphenyl)benzene (H_3BTB) and Co $(NO_3)_2$ (Fig. 9a).[115] The encapsulated Rubpy had a shorter lifetime of 9.5 ns relative to a 600 ns time constant for the pristine Rubpy and this quenching was attributed to a PCT between the ^{3}MLCT of Rubpy to the Co ion cluster of the node with a $k_{CT} \simeq 10^8$ s^{-1} (Fig. 9b). This relatively slow rate constant was due to a high reorganization energy (1.6 eV) and a relatively small (0.006 eV) electronic coupling factor (H_{AB}) as determined from a temperature dependent lifetime data (Fig. 9b) analyzed in Arrhenius fashion.

This group also extended this ship-in-a-bottle fashion strategy in another system where they co-encapsulated two por-

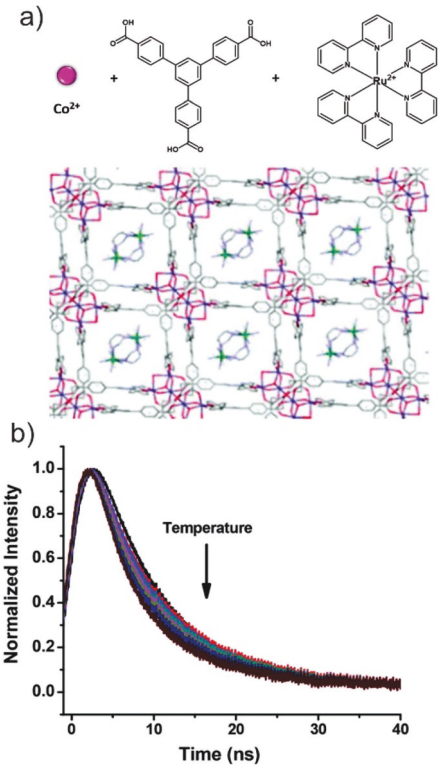

Fig. 9 (a) Scheme of the formation of CoRWLC-2; (b) temperature dependent emission of CoRWLC-2. Reproduced with permission from ref. 115. Copyright 2018, Royal Society of Chemistry.

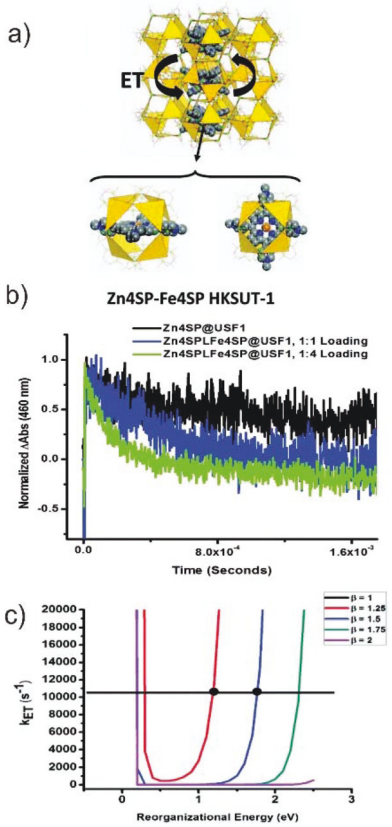

Fig. 10 (a) Scheme illustrating the relative alignment of Zn4SP and HKSUT-1 in Zn4SP@HKUST-1; (b) triplet–triplet absorption decay of Zn4SP@HKUST-1 with varying amounts co-encapsulated Fe4SP suspended in ethanol; (c) plots of calculated k_{ET} *versus* λ for differing β values using d = 29 Å, $k_0 = 1 \times 10^{13}$ s^{-1}, R_0 = 9.7 Å (for Fe4SP/Zn4SP), $\Delta G°$ = −0.61 eV (−14 kcal mol^{-1}) and T = 300 K. The line designates the observed k_{ET} of 11 000 s^{-1}. Reproduced with permission from ref. 116. Copyright 2015, Royal Society of Chemistry.

phyrin derivatives tetrakis-(tetra 4-sulphonatophenyl)porphyrinato zinc(II) (Zn4SP) and tetrakis-(tetra 4-sulphonatophenyl) porphyrinato iron(III) (Fe4SP) into the cages of HKUST-1(Zn) MOF, denoted as Zn4SP-Fe4SP@HKUST-1 (Fig. 10a).[116] The authors reported a PCT from the triplet excited state, ^{3}Zn4SP to Fe4SP ($k_{CT} = 1.1 \times 10^4$ s^{-1}). This was supported by the ^{3}Zn4SP lifetime quenching by the co-encapsulated Fe4SP (Fig. 10b). However, no direct spectroscopic evidence was provided to illustrate the mechanistic evolvement of the triplet states in this complicated photophysical cascade process. The PCT process was analyzed with semi-classical Marcus Theory (eqn (5)) by plotting the rate constant as a function of different sets of parameters:

$$k_{ET} = k_0 e^{-\beta(d-R_0)} e^{-(\Delta G° + \lambda)^2/4\lambda RT} \quad (5)$$

where k_0 is the rate constant associated with barrierless CT at the van der Waals contact distance R_0 between D and A (k_0 typically on the order of a molecular vibration ~10^{13} s^{-1}); β is an empirically determined distance-dependent decay constant for the electronic coupling factor, d is the experimental D–A distance, λ is the total reorganization energy, and $\Delta G°$ is the driving force. A graphical analysis of the experimental data (Fig. 10c) suggested that the observed k_{CT} value can be obtained from three sets of parameters, meaning that eqn (5) has three solutions that could give rise to the observed rate constants (the black dots in Fig. 10c): (a) λ_t = 1.2 eV, β = 1.25; (b) λ_t = 1.75 eV, β = 1. 5; and (c) λ_t = 2.35 eV, β = 1.75. The physical interpretation of these parameters suggests that the λ_t of 2.35 eV (set c) represents considerable structural reorganization that is not likely to occur in the confined octahedral cavities of the MOF, whereas the parameter sets (a) and (b) can be feasible and precedented in the CT process between porphyrins with a fixed intermolecular distance.

As C_{60} is an excellent electron acceptor, it has been infiltrated into the pores of MOFs as an approach to induce photo/electrical conductivity. Goswami *et al.* have reported that the conductivity of the TBAPy based Zr-MOF NU-901 can be increased substantially upon C_{60} incorporation due to a strong electronic interaction at the ground-state leading to an ET from the pyrene-based linker to C_{60}.[85] The Cramer group computationally studied the PCT between C_{60} and two porphyrin-based pillar-paddlewheel MOFs:[117] Zn_2(TCPB)(DA-ZnP) denoted as DA-MOF (TCPB = 1,2,4,5-tetrakis(4-carboxyphenyl) benzene, DA-ZnP = [5,15-bis[(4-pyridyl)ethynyl]-10,20-diphenyl-porphinato]zinc(II); Fig. 11a) and Zn_2(TCPB)(F-ZnP) (*i.e.* denoted as F-MOF; F-ZnP = [5,15-di(4-pyridyl)-10,20-bis(penta-

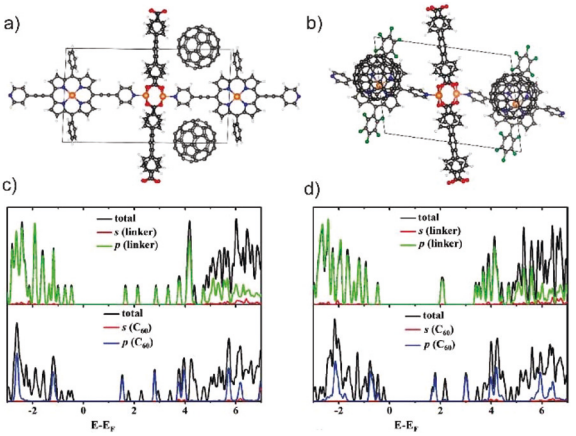

Fig. 11 Optimized crystal structures of (a) C_{60}@DA-MOF; (b) C_{60}@F-MOF; calculated density of states for (c) DA-MOF and (d) F-MOF before (upper panel) and after (lower panel) C_{60} incorporation. The energy is relative to the Fermi level, and the *y* axis for the s- and p-orbitals is scaled by a factor of 1.75. Reproduced with permission from ref. 117. Copyright 2020, American Chemical Society.

fluorophenyl)porphinato]-zinc(II); Fig. 11b). The calculated optical band gaps for DA-MOF and F-MOF are 1.66 and 2.04 eV, respectively. After C_{60} infiltration, C_{60}@DA-MOF (Fig. 11c, lower panels) and C_{60}@F-MOF (Fig. 11d, lower panels) show band gaps that are 0.16 and 0.36 eV lower than their respective pristine DA-MOF and F-MOF. The partial density of states (PDOS) of the C_{60} infiltrated MOFs reveal that the HOCO mainly comprises the p-orbitals of the porphyrin linkers and the LUCO predominantly comprises p-orbitals of C_{60}. The significant orbital overlap between the orbitals of C_{60} and MOF linkers indicates that photoelectrons or holes can be generated on the linkers and should readily transfer to C_{60} at the interfacial region. This study theoretically demonstrated the strategy that the incorporation of the electronic complementary moieties into MOF channels, even without covalent bonding to the framework, can alter the electronic properties of MOF composition that may be used for PCT.

IV. Applications of PCT in MOFs

IV.A. MOF-based photocatalysis

The key point that should be noted from the above discussion is that the compositional versatility that is possible from the wide choice of photoactive struts, metal nodes, and various post-synthetic strategies may allow the development of functional frameworks that are decorated with a plethora of optical or redox components and catalytic species. These inherent design flexibility and molecular scale porosity make MOFs promising photocatalysts. Nevertheless, the intrinsic advantages of a MOF-based design lie in its ability to achieve high substrate and catalyst concentration within the MOF pores in which a PCT between the sensitizer and the catalyst can occur efficiently due to their proximity. Thus, unlike in homogeneous systems, photocatalysis in MOFs is not limited by the diffusion of the catalyst species to the sensitizer, but by the diffusion of the substrate and product. As such, light-driven reactions can be divided mainly into two categories: first, where a sensitizer drives chemical reactions only by an EnT process, like the triplet EnT to drive C–C bond formation (*e.g.* cycloaddition reaction) and reactive oxygen generation that carries out an oxidation reaction of, for example, a mustard gas simulant. The other photocatalysis involves PCT in which one of the photo-generated charges is used to drive single or multi-electron redox reactions. Here, we focus on the second category, *i.e.* the MOF-based photocatalysis that involves PCT. In such reactions, sacrificial reagents are involved to irreversibly regenerate the photosensitizers after every turnover. Sensitized chemical reactions[118] and those driven by the generation of singlet oxygen by MOFs[119–122] do not involve PCT and are therefore excluded from the following discussion.

Transition metals can activate small molecules (*e.g.* H_2O and CO_2) by selective binding and therefore can be used as catalytic sites for energy conversion reactions like the hydrogen evolution reaction (HER) or CO_2 reduction reaction (CRR). A study of a HER process catalytically driven by TiO_2 and titanium-oxo clusters has revealed that a photosensitized CT plays a critical role in high turnover despite its inherent semiconducting nature because TiO_2 is a large-bandgap material corresponding to UV-light ($\lesssim$400 nm) and is less effective to the solar spectrum. The photosensitizer absorbs photons at the visible region of the solar spectrum to drive PCT to the TiO_2 composition if their excited-state oxidation potential lies higher in energy than the TiO_2 conduction band. Following the PCT, the reduced Ti-centers can catalyze the HER.[123,124] The Lin group synthesized two new MOFs, Ti_3-BPDC-Ir and Ti_3-BPDC-Ru (BPDC = biphenyl-4,4′-dicarboxylate), using a mixed linker strategy (Fig. 12a) by which they doped $[Ir(ppy)_2(dcbpy)]^+$ (hereon IrBP) or $[Ru\text{-}(bpy)_2(dcbpy)]^{2+}$ (hereon RuBP) (ppy = 2-phenylpyridine, bpy = 2,2′-bipyridine, and dcbpy = 4,4′-dicarboxy-2,2′-bipyridine) photosensitizers into the Ti_3-BPDC framework which also serves as a catalyst for the HER (Fig. 12b).[125] In these studies, 1,3-dimethyl-2-phenyl-2,3-dihydro-1H-benzo[d]imidazole (BIH) was employed as a sacrificial regenerator (supplier of electrons). To investigate whether the excited photosensitizer was reductively quenched by BIH or oxidatively quenched by $Ti_3(OH)_2$ SBUs, a luminescence quenching experiment for IrBP and RuBP was conducted separately in a homogeneous solution in the presence of BIH or the SBU-equivalent model $Ti_6O_6(OiPr)_6(abz)_6$. The spectroscopic data (Fig. 12d) show that the luminescence of IrBP and RuBP was efficiently quenched by BIH but not by the titanium cluster. This quenching experiment suggests that, in MOFs, the CT proceeds from BIH to the excited IrBP or RuBP forming the reduced IrBP or RuBP species that finally transfer the charge to the Ti-center; the final reduced Ti^{III} is evinced by an EPR signal (Fig. 12e and f). The reduced titanium SBU, Ti^{IV}/Ti^{III}, is responsible for the HER activity. As demonstrated by DFT calculations, this multi-electron LMCT process involves

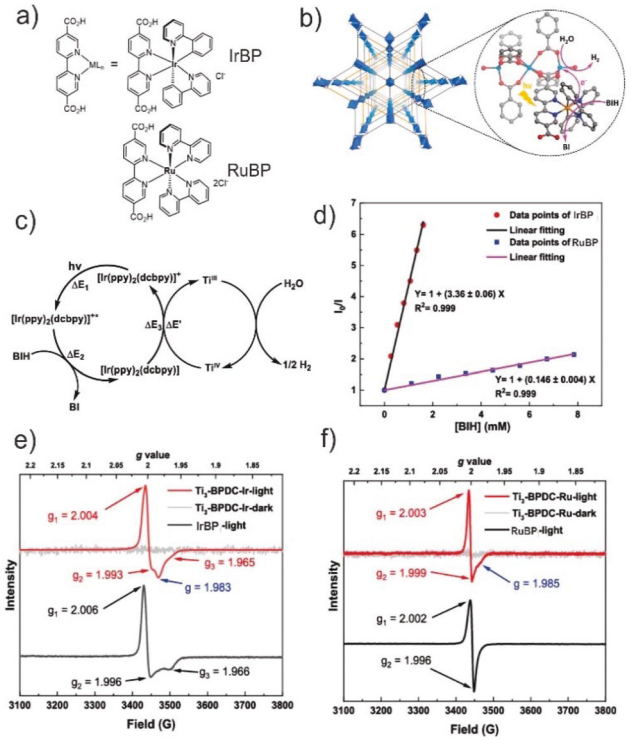

Fig. 12 (a) Synthesis of Ti_3–BPDC–Ir and Ti_3–BPDC–Ru; (b) schematic showing electron injection from photoreduced ligands in $[Ir^{III}(ppy)_2(dcbpy^{-\bullet})]^0$ into $Ti_3(OH)_2$ SBUs to conduct the HER (Ti, Ir, O, and N atoms are shown in blue, gold, red, and mazarine, respectively). (c) Proposed Ti_3-BPDC-Ir catalytic cycle for the light-driven HER, depicting the valence exchange Ti^{III}/Ti^{IV} formed through PCT; (d) Stern Volmer plots of I_0/I for RuBP and IrBP as a function of the concentration of BIH (mM) regenerator. The EPR spectra of (e) Ti_3–BPDC–Ir and (f) Ti_3–BPDC–Ru are shown in the dark or under light irradiation. Reproduced with permission from ref. 125. Copyright 2019, American Chemical Society.

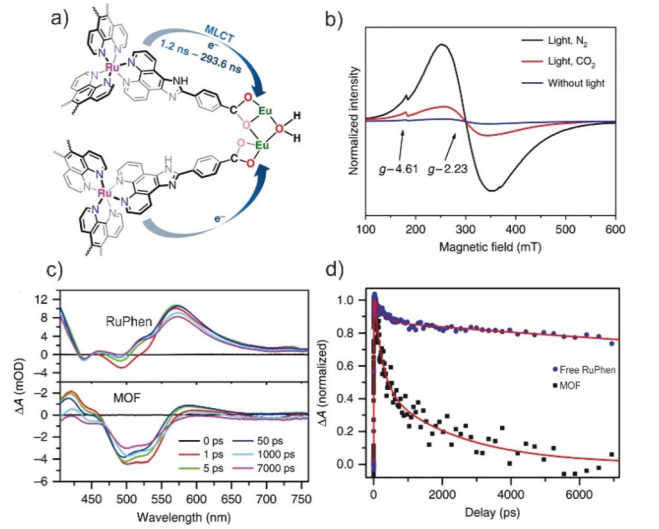

Fig. 13 (a) Schematic showing the PET of Eu–Ru(phen)$_3$–MOF based on the initial excitation of the Ru photocenter and the pathways of ET from Ru to the catalytic Eu_2 oxo-cluster center. (b) *In situ* EPR spectra of Eu–Ru(phen)$_3$–MOF under different conditions; (c) fs-TA spectra of Eu–Ru(phen)$_3$–MOF and H_3L at various time delays at 604 nm; (d) kinetic profile of species traced at 604 nm in free RuPhen and Eu–Ru(phen)$_3$–MOF. Reproduced with permission from ref. 126. Copyright 2018, Nature Publish Group.

the formation of the Ti^{IV}–H intermediate, the rate-determining step with an energy barrier of 0.76 eV in a proton-coupled ET process. The protonation of Ti^{IV} hydride produces H_2 and regenerates the $Ti_3^{IV}(OH)_2$ cluster (Fig. 12c).

In a similar photosensitizer-based design, Yan *et al.* studied a MOF-based PCT involving a Ru(phen)$_3$-derived strut (hereon RuPhen) and Eu^{III} based SBU. The reduced binuclear Eu_2^{II} clusters, generated by exciting RuPhen *via* PCT, serve as catalytic centers for the selective reduction of CO_2 into formate in a two-electron process (Fig. 13a).[126] The PCT process in Eu–Ru(phen)$_3$–MOF was probed *via* fs-TA spectroscopy (Fig. 13c). In contrast to free RuPhen, the ultrafast pump–probe data of the MOF reveal a significant reduction of the ESA amplitude. Excited-state dynamical data (Fig. 13d) suggested a faster ESA decay kinetics of the MOF probed at 604 nm compared to free RuPhen. This faster decay was attributed to the PCT from the T_1 state of the RuPhen species to the Eu clusters. For the catalytic pathway, the authors investigated whether the quenching of RuPhen* proceeds by TEOA reductively or whether an oxidative quenching by the Eu_2 clusters occurs first. For this investigation, luminescence quenching experiments of free RuPhen were carried out in a DMF-solvated form with the addition of TEOA or the Eu_2 clusters separately. A significant quenching by the Eu_2 clusters was observed rather than TEOA; this finding reflects an oxidative CT from RuPhen* to the low-lying orbitals of the Eu_2^{III} clusters as a viable route. This oxidative PCT involving the metal SBU is different from the reductive PCT with the sacrificial reagent observed in Lin's work. The two EPR signals (Fig. 13b) of the Eu–Ru(phen)$_3$–MOF with g = 2.23 and 4.16 revealed the existence of paramagnetic Eu^{2+} species derived from the one-electron reduction of Eu^{3+} that has no EPR response. While the authors did not present any further spectral evidence, their DFT computations suggest that the photocatalytic process involves an exposed Eu^{III} site that adsorbs one CO_2 *via* Eu–O binding. The reduction of the CO_2-Eu intermediate can be efficiently driven by the PCT with an impressive rate of 321.9 μmol h^{-1} mmol MOF^{-1}.

Both Lin's and Yan's works employed noble-metal (*i.e.* Ir or Ru)-based complexes as photosensitizers with different metal SBUs serving as the catalytic centers – their choices depended on the targeted reactions (*i.e.* HER or CO_2 reduction as the driving potential for these transformations is different). It is interesting to note that the PCT sequence in two different MOFs occurred through different pathways, from the excited sensitizer, one involving ET to the node, and the other involving a hole transfer to the redox regenerator. Such a mechanistic difference often stems from the difference in the rate. The factors that play a critical role in determining the rate include the thermodynamic driving force, reorganization energy, and

electronic coupling. The underlying reason may arise from the difference in the electronic properties of metal nodes and sacrificial reagents including their redox potentials. Considering that the charge carrier states are merely localized, the redox potentials measured for the MOFs often represent the frontier orbitals of the monomeric species. For example, the electrochemical data presented in Lin's work suggest that the HOCO (the IrBP centered oxidation) is at 1.49 V, which is 1.16 V more positive than the BIH^+/BIH potential (0.33 V). In contrast, the Ti^{IV}–OH/Ti^{III}–OH potential (*ca.* −0.63 V) species lies only ~0.1 V more positive than the LUCO of the MOF photosensitizer.[125] This can also be visualized from the excited-state redox potentials of a related IrBP compound, where $E_{ox}^{Ir^*}$ = −0.61 V (*vs.* NHE; the reported value of −0.85 V *vs.* SCE)[127] and this should not provide much driving force for PCT to Ti^{IV}–OH/Ti^{III}–OH (*ca.* −0.63 V). Alternatively, $E_{red}^{Ir^*}$ = +0.92 V, which is significantly positive than the BIH^+/BIH potential (0.33 V). It is interesting to note that excited IrBP* sensitizers are well known to get reductively quenched (by a sacrificial reagent) to generate a strong $IrBP^-$ reductant.[128–130] For Yan's Eu–Ru(phen)$_3$–MOF, the potential energy difference between $E_{ox}^{Ru^*}$ (= −0.72 V *vs.* NHE; determined by subtracting the emission energy of 2.07 eV (*i.e.* $E_{0,0}$ at 598 nm maxima) from the oxidation potential of 1.35 V)[126,127] and the conduction band of Eu_2O_3 (−0.68 V) is sufficient to drive the PCT from RuPhen* to Eu-SBU. In contrast, $E_{red}^{Ru^*}$ = +0.78 V (*vs.* NHE; determined by adding 2.07 eV of $E_{0,0}$ to the reduction potential of −1.29 V) renders not much potential energy difference with $TEOA^+$/TEOA (*ca.* 0.81–1.07 V)[131–133] to drive a spontaneous PCT. While these energetics measured for their corresponding models in homogeneous solutions explains the trend, one should recognize that the adopted regional geometry, close spatial separation between the exact complementary pairs, might be different in MOFs to facilitate PCT more efficiently (or less) than predicted in homogeneous solution (or solvent-dispersed) systems.

Using the $Ru(bpy)_3^{2+}$ derivative as the photosensitizer, Lin and coworkers assembled a relatively long analog, bis(2,2′-bipyridine)[5,5′-di(4-carboxyl-phenyl)-2,2′-bipyridine]ruthenium(II) dichloride (hereon RuBPP) together with Hf_{12} SBUs to form a 3D framework denoted as Hf_{12}-Ru.[134] A postsynthesis method was employed to install a secondary carboxy-appended bipyridine complex, $M^I(MeMBA)(CO)_3X$ (M = Re, Mn; MeMBA = methyl 2-(5′-methyl-[2,2′-bipyridin]-5-yl)acetate), onto the Hf_{12} SBUs. This SALI-like functionalization fixes the key components in proximity (the distance between the RuBPP photosensitizer strut and the adjacent $M^I(bpy)(CO)_3X$ catalysts is *ca.* 13 Å) to efficiently drive PCT. Note that this class of organometallic compounds are well-established homogeneous catalysts that bind CO_2 and drive the photocatalytic production of CO (98% selectivity) by accepting an electron from the RuBPP* photosensitizers (Fig. 14).[135–137] While no direct spectroscopic evidence was provided, the authors, in a separate homogeneous quenching test with the model components of Hf_{12}–Ru MOF, found that the phosphorescence of the RuBPP strut got more efficiently quenched by the sacrificial BIH regenerator than by the electron acceptor $M^I(bpy)(CO)_3X$. It is therefore presumed that the reduced $[Hf_{12}–Ru]^-$species, produced from a reductive PCT by BIH, is responsible for preparing the active form of $M^I(bpy)(CO)_3X$ for CO_2 reduction. The authors further reasoned that the first reduction potential of the RuBPP component (−0.65 V *vs.* NHE) is sufficiently reductive than the LUMO of $Re(MeMBA)(CO)_3Cl$ (0.10 V) to convert its active form. However, the PCT here involved *RuBPP and BIH; $E_{red}^{RuBPP^*} \simeq +0.92$ V[127] is significantly positive than the BIH^+/BIH potential (0.33 V)[125,138] to drive the PCT.

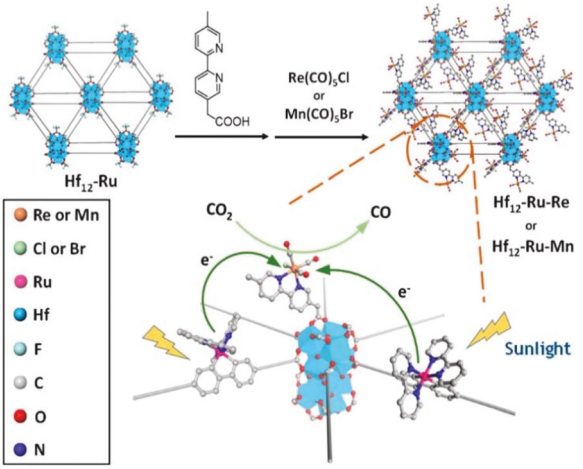

Fig. 14 Schematic illustration of the synthesis of Hf_{12}–Ru–M (M = Re or Mn) *via* monocarboxylic acid exchange of Hf_{12}–Ru and sunlight-driven CO_2 reduction through a mechanism of PET from RuBPP* to $M^I(bpy)(CO)_3X$ (M = Re, Mn) that serves as catalytic sites binding with CO_2. Reproduced with permission from ref. 134. Copyright 2018, American Chemical Society.

An interesting concept of organic transformation involving C–C bond formation was reported by the Duan group using a hybrid crystalline framework (named InP-1). The InP-1 MOF was constructed from L-pyrrolidin-2-ylimidazole (L-PYI, a chiral organocatalyst) and 4,4′,4″-nitrilotrisbenzoicacid (H_3NTB, a photosensitizer)[139] with a twofold interpenetrated framework structure (Fig. 15a) in which the L-PYI and H_3NTB components are proximally arranged in space (Fig. 15b). Within each of the identically isolated chiral frameworks, the Zn(II) ions at the node were coordinated in a chiral tetrahedral geometry with three carboxylate oxygen atoms from three different NTB^{3-} linkers and one nitrogen atom from the L-PYI co-ligand. The photocatalyst exhibits excellent activity for the β-arylation of aldehyde derivatives (Fig. 15c). The photocatalytic process starts with the H_3NTB* photosensitizer that reduces one of the reactants 1,4-dicyanobenzene (DCB) into a radical form $DCB^{\bullet-}$ *via* PCT (Fig. 15d(i)). The resulting $NTB^{\bullet+}$ is then quickly regenerated/reduced by the enamine intermediate that is bound to L-PYI forming an enaminyl radical cation (Fig. 15d(ii)), which then reacts with the $DCB^{\bullet-}$. Here, both the electron acceptor in the PCT and the regenerator are reactants of the catalytic conversion, where a cascade consisting of PCT followed by CT events is facilitated by the proximity of the key components

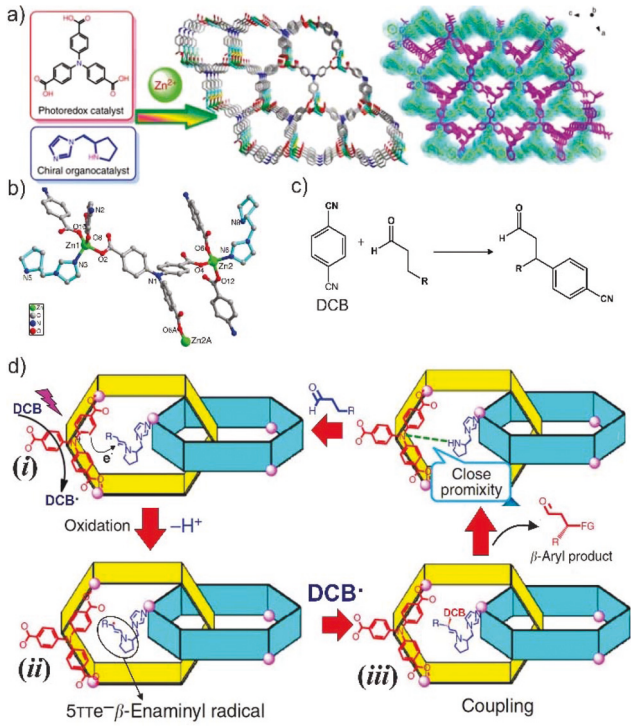

Fig. 15 (a) Chemical structures of the interpenetrated InP-1 MOF and its components; (b) coordination environments of the Zn(II) ions and NTB^{3-} linker; (c) the net β-arylation reaction of saturated aldehydes; (d) proposed mechanisms for interpenetrated MOFs in photocatalytic β-carbonyl activation, showing the PCT pathway and the formation of radical intermediates. Reproduced with permission from ref. 139. Copyright 2017, Nature Publish Group.

L-PYI and H_3NTB (Fig. 15b). The PCT from H_3NTB^* to DCB is probed by the luminescence quenching experiment showing a lifetime drop of H_3NTB from 4.62 to 3.25 ns.

IV.B. Photoelectrochemical processes in MOFs

MOFs can be an ideal platform for facile PCT and related processes; recalling that the chromophore assemblies in MOFs exert antenna behavior, the D/A ratio as well as the concentration of the catalyst moieties can also be widely varied. However, a photocatalytic activity would require an equivalent amount of redox quenchers to regenerate the sensitizer. Instead, the excitons can be delivered to a catalytic center or external electrical contacts, where the charge-carrier generation can be spontaneously driven by the local potential difference. The short-lived excited states and the rapid recombination of the charge carriers seem to be major challenging factors for utilizing the photo-generated redox equivalents (*i.e.* charge with appropriate potential) and hence a limited catalytic efficiency is achieved. In a photoelectrochemical process, the opposite (residual) charges also need to be transported either for catalytic utilization or to be collected at the external electrical contact. Because common metal–carboxylate (or metal/N-base) connectivity involves charge carriers that are localized either at the linkers or at the metal nodes, the charge transport in MOFs involves hopping. The literature reports on charge hopping indicate that the process is diffusion limited by the counter ion.[53,140–143] However, when multiple redox steps are necessary to obtain the active form of catalysts, MOF-incorporated sensitizer (light-harvester) and catalyst assemblies provide a guarantee that major mass-transport related problems can be overcome. Within MOF-based sensitizer-catalyst assemblies, each of the intermediates formed during the progressive transformation of the inactive assembly into an active one would not be susceptible to (a) unwanted diffusion away from a photo-electrode and back into bulk solution, (b) deactivation due to a chemically irreversible encounter, and (c) a physical loss of inadequate solubility and therefore precipitation of the intermediate species. Within a solid assembly, the separation of the electron–hole pair can be promoted either by the electrical field that is spontaneously formed at the interface of the photoelectrode or by an external electrical field to direct electrons and holes to participate in reduction and oxidation reactions before they recombine (Fig. 16).[144–147] In a classic semiconducting band picture, when the n-type semiconductor is employed as the photoelectrode, electrons and holes are formed at the surface by splitting the photo-generated excitons at the surface; the electrons are locally driven to the interior bulk, whereas the holes on the surface spontaneously form a local electrical field – a phenomenon represented by the bending of the band (Fig. 16a).[148] Likewise, the p-type semiconductor (Fig. 16b) forms a regional electrical field pointing toward the opposite direction as the n-semiconductor case. The picture in MOFs, however, is not this simple and universal. Even for a sluggish hopping-mediated

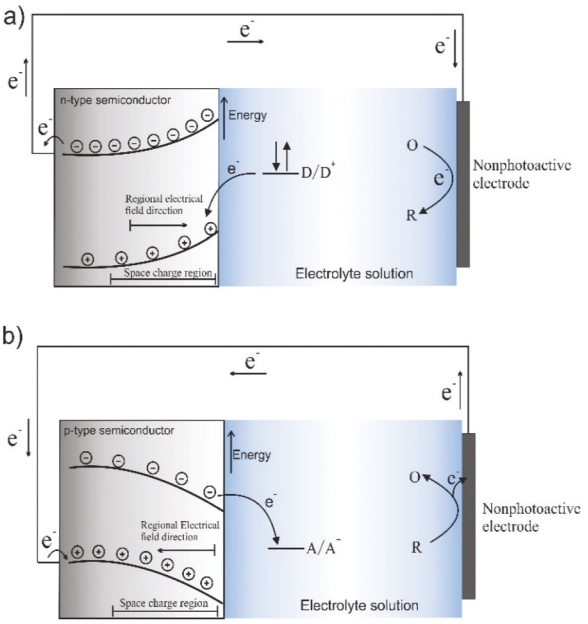

Fig. 16 Scheme of (a) n-type and (b) p-type semiconductor cells, depicting the formation of a space charge region, locally bending bands under irradiation and the direction of electron flow. The interfacial electron transfer between the photoelectrode and D/D^+ or A/A^- species in solution is illustrated too.

charge transport process, charge that hops within MOF crystals deposited on a semiconducting electrode surface (*e.g.* a MOF modified TiO_2-layered-FTO electrode) would feel a similar force field (stemming from the potential energy difference between the semiconductor band edge and the MOF redox potentials concerned) driving a directional transport. Alternatively, exciton splitting can be achieved under an applied bias voltage over the circuit to steer the photogenerated electrons or holes –in such cases, no semiconducting layer is used (*e.g.* a MOF modified FTO electrode).[37]

García-Sánchez *et al.* synthesized a new MOF, called IEF-5, with bismuth and dithieno[3,2-b:2′,3′-d]thiophene-2,6-dicarboxylic acid (DTTDC). They constructed their photoanode by depositing the IEF-5 on ITO; the photoelectrons collected were used to drive the HER at the Pt counter electrode (Fig. 17a).[149] Computational work on PDOS revealed that the IEF-5 has a 2.1 eV bandgap (Fig. 17b). The positive response of the photocurrent (Fig. 17c) indicates an n-type semiconductor. Prior to charge separation, photoexcitation leads to an ultrafast charge redistribution defined by an electron delocalization around sulfur atoms. This process was probed *via* synchrotron Core Hole Clock (CHC) experiments (Fig. 17d), which involve recording the S KLL Auger spectra at different excitation energies around the sulfur K-edge with attosecond time resolution. The charge delocalization time was calculated as 1.27 fs. The optical TA spectra collected for the IEF-5 with a 355 nm pump/white-probe setup show a band at 440 nm with a first-order decay (τ = 25 μs; Fig. 17e) and was attributed to a possible transient absorption in the triplet manifold.

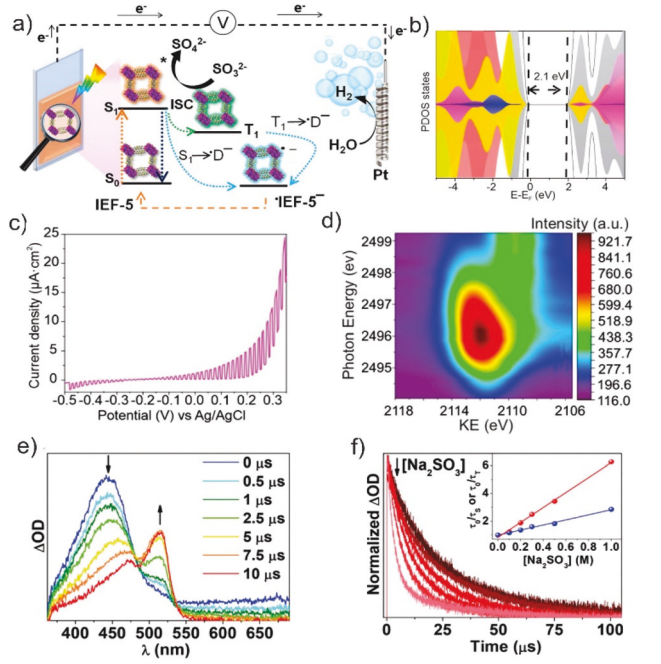

Fig. 17 (a) Scheme of a MOF-based photoelectrochemistry cell for the HER, highlighting the ET through singlet and triplet states; (b) atom-projected partial density of states (PDOS) for Bi 2s (magenta), Bi 2p (blue), C 2p (gray), sulfur (yellow), oxygen (red); (c) LSV under chopped illumination showing the photocurrent density at different bias potentials; (d) 2D core hole clock measurements of IEF-5; (e) TA spectra acquired at different delay time under the excitation of 355 nm for IEF-5 in the presence of Na_2SO_3 as an electron donor. (f) Evolving of the triplet lifetime (λ_{ex} = 355 nm) as the function of concentrations of Na_2SO_3. The inset is the Stern–Volmer plot for singlet (blue) and triplet (red). Reproduced with permission from ref. 149. Copyright 2020, American Chemical Society.

In the presence of a redox quencher such as an electron donor Na_2SO_3 ($E^{2-}_{SO3/SO42-}{}^{0}$ = 0.93 V *vs.* NHE) in the solution, pump–probe experiment displayed TA spectra that highlight quenching of the 440 nm band and the evolution of a new 515 nm transition due to the formation of a radical anion IEF-5$^{\bullet-}$ upon the PCT. The PCT can be described as a reductive quenching of the MOF excited state by SO_3^{2-}. Interestingly, the IEF-5$^{\bullet-}$ signal was no longer detected in an oxygen-saturated solution. The oxygen quenching experiment suggests that the PCT involves ^{3}IEF-5*. The relative contribution of the ^{1}IEF-5* and ^{3}IEF-5* species in the PCT process was determined by a Stern–Volmer analysis. With the $K_{SV(S)}$ of 1.85 and 5.35 M^{-1} for singlet and triplet excited-states, respectively, the authors suggested that the ^{3}IEF-5* is the key driver of the PCT. The photogenerated electrons are transported to the counter electrode performing the HER; a constant H_2 evolution was observed with a 2.35 μmol cm^{-2} gas accumulated within 60 minutes of irradiation.

Morris and coworkers incorporated mixed-linkers including a RuBP photosensitizer and catalytic site $[Ru(tpy)(dcbpy)Cl]^+$ (hereon RuTB; tpy = 2,2′:6′,2″-terpyridine) into UiO-67 MOF as a photoelectrode material (Fig. 18a).[150] A thin MOF film was grown on an n-type semiconducting (TiO_2-coated FTO) electrode serving as a photoanode for the oxidation of alcohol. The proposed mechanism in Fig. 18b shows that electrons are injected to the TiO_2 layer from $Ru^{II}BP$*, thereby generating a hole that forms $Ru^{III}BP$. $Ru^{II}TB$ is subsequently oxidized by $Ru^{III}BP$ forming $Ru^{III}TB$ that finally oxidizes alcohol. This photophysical pathway is demonstrated by the ns-TA spectra, which highlight that the excited state absorption band of RuBP-RuTB-UiO-67-TiO_2/FTO near 420 nm diminishes significantly (Fig. 18c); this was attributed to the charge injection from $Ru^{II}BP$* to the conduction band of TiO_2. The authors observed that the isosbestic point (at ΔO.D. = 0) exhibits a bathochromic shift from 555 to 620 nm over time (Fig. 18c and d) due to a delayed formation of $Ru^{II}TB$* or $Ru^{III}TB$, which could happen in one of the two ways: either the formation of $Ru^{II}TB$* occurs *via* EnT from RuBP* to $Ru^{II}TB$; alternatively, $Ru^{III}TB$ could be formed *via* oxidation by $Ru^{III}BP$ that was formed upon the PCT (to TiO_2, Fig. 18b, step 3). The time-constant (21.0 ± 0.3 ns) for the shift of the isosbestic point was determined from the delayed growth at 550 nm. Based on these experimental data, it seems neither pathway could be ruled out, although the authors preferentially proposed the second process as a dominating route. For such a system, varying the ratio of the primary photosensitizer and the catalysts and/or a solvent-dependent transient spectroscopic measurement may provide further information regarding the preferentially adopted photophysical pathway.

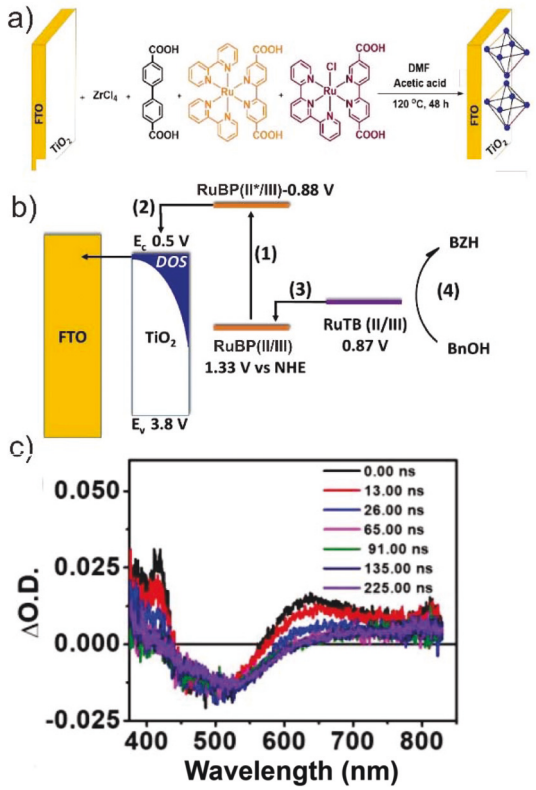

Fig. 18 (a) Schematic representation of a MOF/TiO_2/FTO assembly *via* a direct solvothermal synthesis of the mixed-linker MOF film; (b) energy diagram illustrating the photophysical process at the photoelectrode, including (i) photoexcitation of $Ru^{II}BP$ to $Ru^{II}BP$*; (ii) electron injection from $Ru^{II}BP$* into the conduction band of TiO_2; (iii) oxidation of $Ru^{II}TB$ by $Ru^{III}BP$ to form $Ru^{III}TB$; and (iv) oxidation of benzyl alcohol (BnOH) by $Ru^{III}TB$ to benzaldehyde (BZH); (c) ns-TA spectra of RuBP-RuTB-UiO-67-TiO_2/FTO. Reproduced with permission from ref. 150. Copyright 2020, Royal Society of Chemistry.

As discussed above, MOFs can be used as dye assemblies and can be deposited on a transparent conducting electrode (TCO) such as FTO or ITO. To make the MOF-modified electrode (*i.e.* MOF film deposited/grown on TCO) serve as a photocathode or photoanode, commonly p-type (*e.g.*, NiO) or n-type (*e.g.* TiO_2) large bandgap semiconducting layers are deposited as a barrier (*i.e.* in between the MOF layer and TCO). These semiconducting layers not only facilitate exciton splitting at their interfaces with the dye (here MOF) but also provide an augmented connection that provides charge-carrier doping based on their potential and therefore collects the electron or hole. In contrast, by switching the redox mediator (D or A species) in the electrolyte, the MOF-based photoelectrode can be made to serve as a photoanode or photocathode accordingly. Such fabrication is different from a standard semiconducting layered electrode, because, for the MOF-only system, the kinetics of PCT at the MOF-electrolyte interface dictates the polarity of the MOF-modified electrode. Hod and co-workers demonstrated that the interfacial CT kinetics on the surface of a porphyrin-based MOF-525/FTO photoelectrode could be tuned by introducing electron or hole-accepting species, such as water and triethanolamine (TEOA) into the electrolyte solution (Fig. 19a and b).[37] The introduction of a hole-acceptor TEOA resulted in a photo-anodic response: *i.e.* under light illumination, a positive increment of current density was observed with a shift of the onset oxidation potential from 0.85 V to 0 V (*vs.* NHE; Fig. 19c). In the case of water as the electron acceptor, photo-cathodic behavior was observed upon light illumination, where electrons from the excited MOFs are transferred to protons generating H_2. In the latter case, dark and light LSV measurements exhibit an increasing current density in a negative direction (Fig. 19d), attributed to the PCT from MOF-525* to water. The photo induced oxidation of TEOA to $TEOA^{\bullet+}$ is a fast one-electron process, whereas photo induced reduction of water to H_2 at the photocathode is a relatively and kinetically sluggish 2-electron process. Hence, the photo generated charges spend a longer time at the photocathode, simply increasing its probability to recombine *via* for example, solution charge accepting species.

Zhou *et al.* fabricated a bismuth vanadate electrode covered with porous cobalt and imidazole 'Co-Mim' (Mim = 2-methylimidazole, this Co-Mim is structurally different from ZIF-67) and used this photoanode for water oxidation.[151] At 1.23 V (*vs.* RHE), the $BiVO_4$@Co-MIm electrode emits 2.4 times more photocurrent than the bare $BiVO_4$ electrode (Fig. 20b). The plot of the photogenerated charge separation efficiency (Φ_{sep}) as a function of applied potential suggests that $BiVO_4$@Co-MIm exhibits a higher Φ_{sep} compared to the pristine $BiVO_4$ in the entire range (Fig. 20c). Here, $\Phi_{sep} = J_{sep}/J_{abs}$; where J_{sep} is the current density measured in the electrolyte containing hole trapping agent (Na_2SO_3) and J_{abs} is the maximum theoretical current density. The author suggests that the cobalt ion suppresses the recombination of the holes reaching the surface, thus promoting hole injection to the electrolyte by

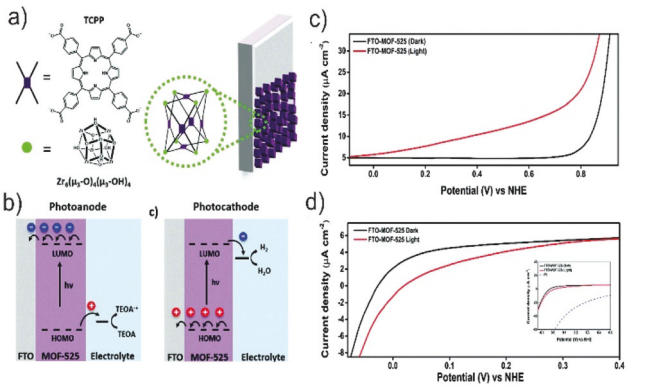

Fig. 19 (a) The components for MOF-525 assembly and the fabrication of a photoelectrode; (b) scheme illustration of the PET at the photoanode and photocathode fabricated from MOF-525, in the presence of TEOA as D or H_2O as A respectively; LSV curves for MOF-525 (c) photoanode (*i.e.* TEOA in solution as donor species) and (d) photocathode (*i.e.* H_2O as an electron acceptor) in the dark (black) and under light (red). Reproduced with permission from ref. 37. Copyright 2019, Royal Society of Chemistry.

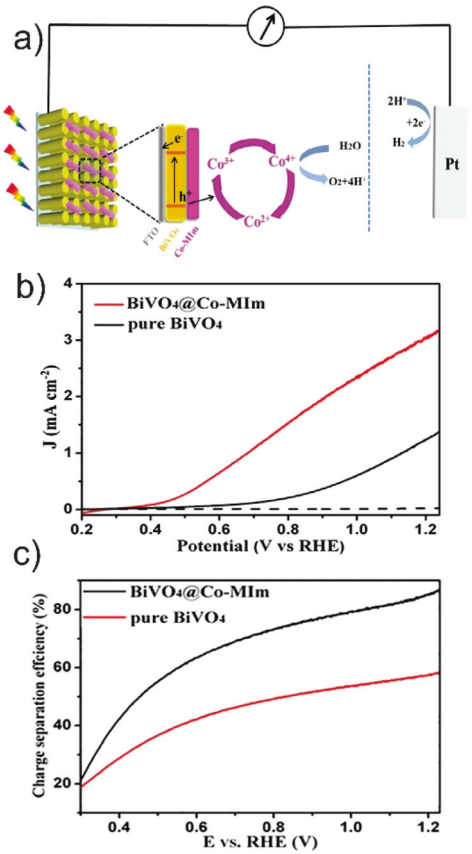

Fig. 20 The proposed photogenerated charge generation, transport, and water splitting reaction at the $BiVO_4$@Co-MIm anode; (b) LSV curves of the $BiVO_4$ and $BiVO_4$@Co-MIm electrodes under illumination, the dotted line is the LSV curve of $BiVO_4$@Co-MIm without illumination for comparison; (c) charge separation efficiency of $BiVO_4$ and $BiVO_4$@Co-MIm electrodes at different potentials. Reproduced with permission from ref. 151. Copyright 2019, Elsevier.

creating an energy barrier for the hole to recombine. Fig. 20a shows the proposed mechanism of water oxidation. Under light illumination, $BiVO_4$ would be excited to produce the photogenerated electron–hole pairs, where the hole transfer to the Co-Mim layers takes place to generate Co^{3+} and then Co^{4+} – the active form of the catalysts driving the water oxidation. The OER reaction converts the Co^{4+} back to Co^{2+}. The electrons collected at the photoanode from the reduced $BiVO_4$ are transported to the Pt counter electrode to drive the HER. It is intriguing to note that the aligned $BiVO_4$ nanostructures have a large surface area with micrometer-scale pores; the Co–MIm is solvothermally grown on the surface of the $BiVO_4$ nanostructure; thus, the separated charges may not necessarily need to travel significant distances. Furthermore, the deposited Co-MIm component does not seem to contribute to the visible light absorption possibly due to its thin layer morphology. Even though this study specifically did not provide much spectroscopic evidence, the improvement in the photocurrent indicates the involvement of the porous Co-MIM as the hole transport layer through PCT. This design may inspire further development of the MOF based OER system in conjunction with molecular (RuBP, RuPhen, IrBP, *etc.*) or desired metal–oxide sensitizers.

IV.C. MOF-based luminescence sensing

MOFs have been explored as working compositions for sensing applications due to the tunable luminescence properties originating from the linkers and their interactions with secondary species including metallic nodes and guest species.[27,152–158] The attractive feature in these frameworks is the arrays of binding sites available for the analytes. These binding sites can be installed post-synthetically if not present in the pristine form. The fluorophore/luminophore in MOFs undergoes radiative recombination decay from the excited state (*i.e.* L*), which gets quenched when L* gets involved in a PCT reaction. Thus, the extent of the emission quenching in MOFs can be a function of analyte concentration.[27,159] These turn-off sensors are common and maybe less selective since they can be susceptible to the introduction of various non-radiative decay pathways, which consequently leads to false reporting.[160] In contrast, turn-on sensors require selective binding with analytes and therefore, we only focus on those MOF-based systems in which the analytes turn the sensor from non-emissive to emissive form *via* a PCT; note that an EnT based turn-on system is also possible, where the analytes switch off a pre-existing internal D–A based EnT to recover the emission of D – but we are not discussing those.

The Qian group reported ZJU-109 -a cobalt-based mix linker MOF prepared from 2-(4-pyridyl)-terephthalic acid (H_2PTA) and 4,4′-bis(imidazolyl)biphenyl (4,4′-bimbp) -which is employed as a turn-on sensor for the Fe^{3+} ion.[161] Without Fe^{3+}, the PCT proceeds from the 4,4′-bimbp* (acting fluorophore) to the PTA acceptor. This efficient PCT precludes the fluorescence of the linker 4,4′-bimbp (Fig. 21a). With the help of DFT calculations, the authors predicted that Fe^{3+} binding to PTA^{2-} forms Fe-PTA species with an iron-centered highly stabilized lowest unoccupied orbital (−5.5 eV), which is close in energy to its modified and destabilized valence orbitals (*ca.* −5.8 eV). Thus, the high energy gap from E_{ox}^{bimbp*} and the lowest unoccupied orbital of Fe-PTA attenuates the PCT efficiency (Fig. 21b). Increase in driving force can effectively reduce the CT-rate if the process is in the Markus inverted region (*i.e.* $|\Delta G°| > \lambda_t$). The authors attributed the recovery of 4,4′-bimbp emission to the blocked ET from 4,4′-bimbp* to Fe-PTA.

Using the mixed-ligand strategy, Gui and coworkers reported the Zr-based UiO-68-An/Ma MOFs with anthracene and maleimide -based mixed linkers as the sensor of biothiols (Fig. 22a).[162] The low photoluminescence quantum yield (QY = 1.1%) of UiO-68-An/Ma indicates the fluorescence quenching of anthracene by maleimide through PCT. As shown in the bright-field luminescent images (Fig. 22b), the QY of UiO-68-An/Ma is recovered to 28.1% when it was exposed to 2-mercaptoethanol that is chemisorbed/trapped with the Ma-component forming UiO-68-An/TE (TE = thiol–ene adduct of the Ma); likewise, a 22.0% QY was observed when exposed to 3-furanmethanol forming UiO-68-An/DA (DA = diels–alder product).

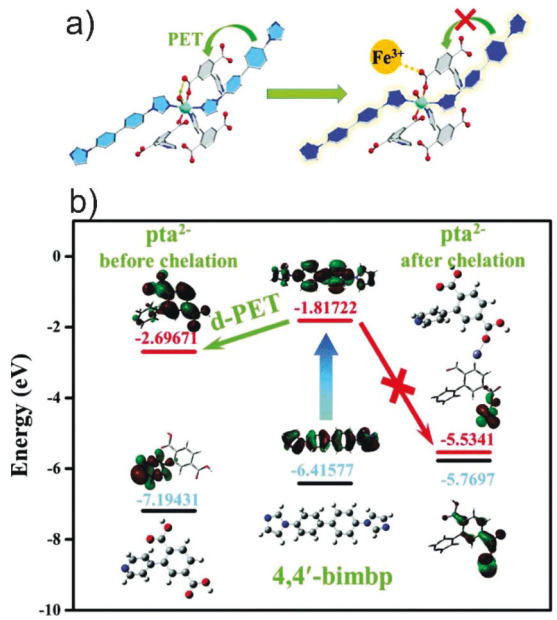

Fig. 21 (a) Schematic illustration of the PET process and the turn-on sensing of Fe^{3+}; (b) calculated HOMO and LUMO energy levels of 4,40-bimbp and H2PTA pta^{2-} and the PET pathway between the two species. The binding of Fe^{3+} to pta^{2-} energetically hindered PET. Reproduced with permission from ref. 161. Copyright 2019, Royal Society of Chemistry.

The binding of 2-mercaptoethanol or 3-furanmethanol onto Ma switched off the PCT from An* to Ma, thus An* could return to the ground state through a radiative process. This special combination of the two chromophores within a framework realizes a tunable PCT by selective binding with the analytes, which enables UiO-68-An/Ma to serve as a sensor for biothiols.

An alternative approach to tune the efficiency of the PCT between the chromophores and the neighboring (MOF bound/assembled) quencher can be achieved by knocking out the quenchers *via* a competitive coordination with the analyte. Li *et al.* synthesized a coordination network that features aggregation-induced emission (AIE) displayed by the assembled hydroxyl-functionalized ligand 4,4′-((Z,Z)-1,4-diphenylbuta-1,3-diene-1,4-diyl)bis(2-hydroxybenzoic acid) (HTABDC) and Zn (II)[163] (Framework 1 = F1). When this zigzag coordination network was combined with 4,4′-bipyridine (Bpy) pillar, it formed a porous 3D network (Framework 2 = F2). However, the AIE of the HTABDC linker, observed in F1, was quenched in F2 by the auxiliary Bpy linker. This quenching was attributed to a facile PCT between HTABDC* and Bpy as the latter component has the LUMO that lies 1.4 eV lower than that of HTABDC (Fig. 23a). When this F2 assembly was exposed to Al^{3+} (a specific analyte), the ion gets preferentially chelated by the

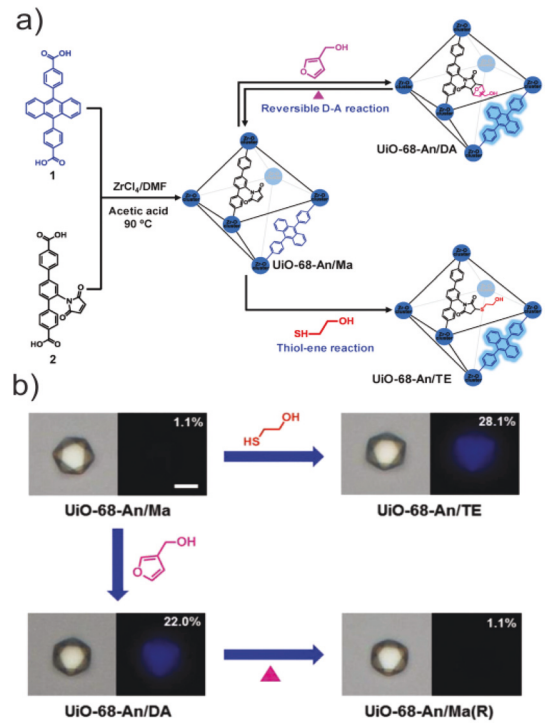

Fig. 22 (a) Synthesis of UiO-68-An/Ma and tuning the fluorescent PET in the MOF through a reversible D–A reaction or thiol–ene reaction; (b) bright-field and photoluminescence images of fresh UiO-68-An/Ma, UiO-68-An/DA, UiO-68-An/Ma(R) excited by a mercury lamp, and UiO-68-An/TE. Reproduced with permission from ref. 162. Copyright 2018, Wiley-VCH.

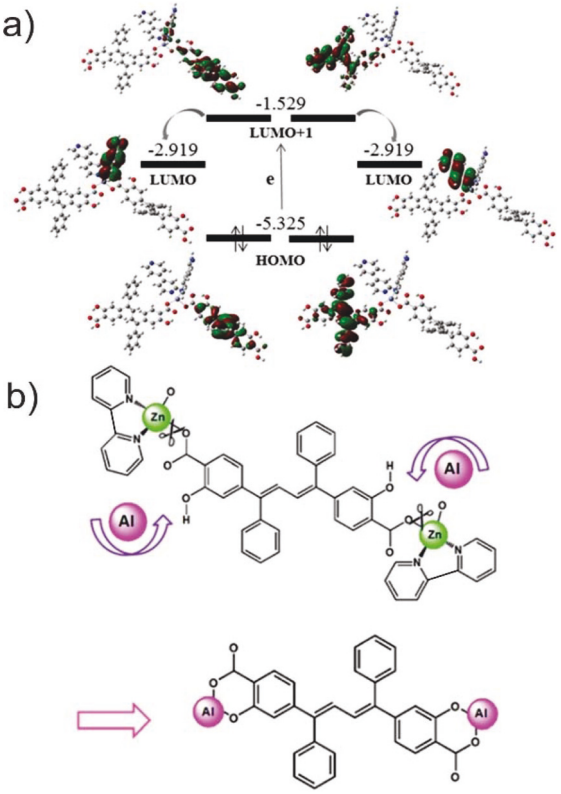

Fig. 23 (a) Diagram of a photoinduced electron transfer from ligands HTABDC to Bpy in Framework 2, indicating a lower LUMO orbital of Bpy than the S_1 of HTABDC. (b) Schematic representation of the competitive coordination between Al^{3+} and Zn^{2+} with HTABDC. Reproduced with permission from ref. 163. Copyright 2018, American Chemical Society.

2-hydroxycarboxylate moiety of the HTABDC; as a result, the F2 MOF gets dissociated (Fig. 23b). The author claims that F2 dissociation leads to the removal of Bpy, which, in turn, shuts down the PCT between the two types of linkers. Thus, the new aggregation of Al-HTABDC leads to the recovery of AIE (*i.e.* the fluorescence is switched on). Interestingly, ~3 ppb (less than the 200-ppb limit set by US-EPA) of Al^{3+} was found sufficient to release enough bpy that makes this AIE recovery optically (visually) detectable. With these few examples presented above, we can clearly say that superior turn-on sensors can be developed in MOFs by suppressing the PCT between the internal components as the 'switching off' mechanism upon a selective analyte binding.

V. Conclusion and future perspective

The inherently modular yet precise organization of optoelectronically active species can render a solid compositional platform where PCT can be tuned by virtue of its ground and excited-state potential and the distance fixed within the frameworks. Such an organization also offers unique opportunities to vary the ratio of sensitizer to acceptor or sensitizer to catalyst, with or without the energy transport bridge. The basic function of MOFs can be versatile, such as sensitizer and light-harvester that can host or incorporate organized molecular interfaces for charge transfer and subsequent transport for their utilization at a catalytic center or recovery at the external electrical contacts. The precise organization of the desired photoactive species around well-defined pores not only defines the controlled evolution of the photophysical properties but also does so in a more efficient way, different from what we see in typical molecular aggregates. All these features are key requirements for photocatalysis and photoelectrocatalysis, where understanding the key steps and devising ways to control them can lead to the development of high performing working compositions. Photoinduced charge (both electrons and holes) transfer is only a key middle step here, which requires excitation energy to be efficiently delivered to the exciton splitting interface and the ability after carrying the generated redox equivalents (charge with the appropriate potentials) to the desired place.

Both theoretical and experimental works were presented here to systematically demonstrate the strategy adopted for probing PCT and its efficient applications. Thus, the appropriate choice of the complementary units and their assembly will define key tools to prolong the exciton lifetime, and slowing the electron–hole recombination, possibly by carrying them far, should be part of future developments to improve the photo- and photoelectrocatalytic reactions. For these, one key step is laying the fundamental platform for long-range directional energy and charge transport processes. Once such strategies are adopted in robust MOFs, the system can be diversified with the tailored components for the desired usage. For this, post-synthesis approaches simply widen the horizon of possibilities.

Conflicts of interest

There are no conflicts to declare.

Acknowledgements

P. D. gratefully acknowledges funding from the National Science Foundation (NSF CAREER CHE-1944903). X. L. and J. Y. acknowledge the dissertation research award through graduate school, SIUC.

Notes and references

1 J. R. Long and O. M. Yaghi, The Pervasive Chemistry of Metal–Organic Frameworks, *Chem. Soc. Rev.*, 2009, **38**(5), 1213–1214.
2 H.-C. Zhou, J. R. Long and O. M. Yaghi, Introduction to Metal–Organic Frameworks, *Chem. Rev.*, 2012, **112**(2), 673–674.
3 M. O'Keeffe and O. M. Yaghi, Deconstructing the Crystal Structures of Metal–Organic Frameworks and Related Materials into Their Underlying Nets, *Chem. Rev.*, 2012, **112**(2), 675–702.
4 W. Lu, Z. Wei, Z.-Y. Gu, T.-F. Liu, J. Park, J. Park, J. Tian, M. Zhang, Q. Zhang, T. Gentle Iii, M. Bosch and H.-C. Zhou, Tuning the Structure and Function of Metal–Organic Frameworks Via Linker Design, *Chem. Soc. Rev.*, 2014, **43**(16), 5561–5593.
5 Y. Bai, Y. Dou, L.-H. Xie, W. Rutledge, J.-R. Li and H.-C. Zhou, Zr-Based Metal–Organic Frameworks: Design, Synthesis, Structure, and Applications, *Chem. Soc. Rev.*, 2016, **45**(8), 2327–2367.
6 J.-R. Li, Y. Ma, M. C. McCarthy, J. Sculley, J. Yu, H.-K. Jeong, P. B. Balbuena and H.-C. Zhou, Carbon Dioxide Capture-Related Gas Adsorption and Separation in Metal-Organic Frameworks, *Coord. Chem. Rev.*, 2011, **255**(15), 1791–1823.
7 J.-R. Li, R. J. Kuppler and H.-C. Zhou, Selective Gas Adsorption and Separation in Metal–Organic Frameworks, *Chem. Soc. Rev.*, 2009, **38**(5), 1477–1504.
8 S. Ma and H.-C. Zhou, Gas Storage in Porous Metal–Organic Frameworks for Clean Energy Applications, *Chem. Commun.*, 2010, **46**(1), 44–53.
9 L. J. Murray, M. Dincă and J. R. Long, Hydrogen Storage in Metal–Organic Frameworks, *Chem. Soc. Rev.*, 2009, **38**(5), 1294–1314.
10 M. Dincă and J. R. Long, Hydrogen Storage in Microporous Metal–Organic Frameworks with Exposed Metal Sites, *Angew. Chem., Int. Ed.*, 2008, **47**(36), 6766–6779.
11 Z. Chen, P. Li, R. Anderson, X. Wang, X. Zhang, L. Robison, L. R. Redfern, S. Moribe, T. Islamoglu, D. A. Gómez-Gualdrón, T. Yildirim, J. F. Stoddart and O. K. Farha, Balancing Volumetric and Gravimetric

Uptake in Highly Porous Materials for Clean Energy, *Science*, 2020, **368**(6488), 297–303.

12 R. Kaur, K.-H. Kim, A. K. Paul and A. Deep, Recent Advances in the Photovoltaic Applications of Coordination Polymers and Metal Organic Frameworks, *J. Mater. Chem. A*, 2016, **4**(11), 3991–4002.

13 D. Y. Lee, C. Y. Shin, S. J. Yoon, H. Y. Lee, W. Lee, N. K. Shrestha, J. K. Lee and S.-H. Han, Enhanced Photovoltaic Performance of Cu-Based Metal-Organic Frameworks Sensitized Solar Cell by Addition of Carbon Nanotubes, *Sci. Rep.*, 2014, **4**(1), 3930.

14 D. Y. Lee, D. V. Shinde, S. J. Yoon, K. N. Cho, W. Lee, N. K. Shrestha and S.-H. Han, Cu-Based Metal–Organic Frameworks for Photovoltaic Application, *J. Phys. Chem. C*, 2014, **118**(30), 16328–16334.

15 T. Zhang and W. Lin, Metal–Organic Frameworks for Artificial Photosynthesis and Photocatalysis, *Chem. Soc. Rev.*, 2014, **43**(16), 5982–5993.

16 A. Dhakshinamoorthy, A. M. Asiri and H. García, Metal–Organic Framework (MOF) Compounds: Photocatalysts for Redox Reactions and Solar Fuel Production, *Angew. Chem., Int. Ed.*, 2016, **55**(18), 5414–5445.

17 H.-Q. Xu, J. Hu, D. Wang, Z. Li, Q. Zhang, Y. Luo, S.-H. Yu and H.-L. Jiang, Visible-Light Photoreduction of CO_2 in a Metal-Organic Framework: Boosting Electron-Hole Separation Via Electron Trap States, *J. Am. Chem. Soc.*, 2015, **137**(42), 13440–13443.

18 H. Li, Y. Yang, C. He, L. Zeng and C. Duan, Mixed-Ligand Metal-Organic Framework for Two-Photon Responsive Photocatalytic C-N and C-C Coupling Reactions, *ACS Catal.*, 2019, **9**(1), 422–430.

19 J.-D. Xiao, L. Han, J. Luo, S.-H. Yu and H.-L. Jiang, Integration of Plasmonic Effects and Schottky Junctions into Metal-Organic Framework Composites: Steering Charge Flow for Enhanced Visible-Light Photocatalysis, *Angew. Chem., Int. Ed.*, 2018, **57**(4), 1103–1107.

20 Y. Zhang, J. Pang, J. Li, X. Yang, M. Feng, P. Cai and H.-C. Zhou, Visible-Light Harvesting Pyrene-Based Mofs as Efficient Ros Generators, *Chem. Sci.*, 2019, **10**(36), 8455–8460.

21 C. Wang, Z. Xie, K. E. de Krafft and W. Lin, Doping Metal–Organic Frameworks for Water Oxidation, Carbon Dioxide Reduction, and Organic Photocatalysis, *J. Am. Chem. Soc.*, 2011, **133**(34), 13445–13454.

22 L. E. Kreno, K. Leong, O. K. Farha, M. Allendorf, R. P. Van Duyne and J. T. Hupp, Metal–Organic Framework Materials as Chemical Sensors, *Chem. Rev.*, 2012, **112**(2), 1105–1125.

23 Y. Cui, R. Song, J. Yu, M. Liu, Z. Wang, C. Wu, Y. Yang, Z. Wang, B. Chen and G. Qian, Dual-Emitting Mof ⊃ Dye Composite for Ratiometric Temperature Sensing, *Adv. Mater.*, 2015, **27**(8), 1420–1425.

24 X. Zhu, H. Zheng, X. Wei, Z. Lin, L. Guo, B. Qiu and G. Chen, Metal–Organic Framework (MOF): A Novel Sensing Platform for Biomolecules, *Chem. Commun.*, 2013, **49**(13), 1276–1278.

25 B. Gole, A. K. Bar and P. S. Mukherjee, Fluorescent Metal–Organic Framework for Selective Sensing of Nitroaromatic Explosives, *Chem. Commun.*, 2011, **47**(44), 12137–12139.

26 S.-P. Yang, W. Zhao, P.-P. Hu, K.-Y. Wu, Z.-H. Jiang, L.-P. Bai, M.-M. Li and J.-X. Chen, Lanthanum-Based Metal-Organic Frameworks for Specific Detection of Sudan Virus Rna Conservative Sequences Down to Single-Base Mismatch, *Inorg. Chem.*, 2017, **56**(24), 14880–14887.

27 X.-D. Zhu, K. Zhang, Y. Wang, W.-W. Long, R.-J. Sa, T.-F. Liu and J. Lu, Fluorescent Metal-Organic Framework (MOF) as a Highly Sensitive and Quickly Responsive Chemical Sensor for the Detection of Antibiotics in Simulated Wastewater, *Inorg. Chem.*, 2018, **57**(3), 1060–1065.

28 Z. Wang and S. M. Cohen, Postsynthetic Modification of Metal–Organic Frameworks, *Chem. Soc. Rev.*, 2009, **38**(5), 1315–1329.

29 T. M. McDonald, D. M. D'Alessandro, R. Krishna and J. R. Long, Enhanced Carbon Dioxide Capture Upon Incorporation of N,N′-Dimethylethylenediamine in the Metal-Organic Framework Cubttri, *Chem. Sci.*, 2011, **2**(10), 2022–2028.

30 M. Kim, J. F. Cahill, H. Fei, K. A. Prather and S. M. Cohen, Postsynthetic Ligand and Cation Exchange in Robust Metal–Organic Frameworks, *J. Am. Chem. Soc.*, 2012, **134**(43), 18082–18088.

31 S. M. Cohen, Postsynthetic Methods for the Functionalization of Metal–Organic Frameworks, *Chem. Rev.*, 2012, **112**(2), 970–1000.

32 T. Li, M. T. Kozlowski, E. A. Doud, M. N. Blakely and N. L. Rosi, Stepwise Ligand Exchange for the Preparation of a Family of Mesoporous MOFs, *J. Am. Chem. Soc.*, 2013, **135**(32), 11688–11691.

33 O. Karagiaridi, W. Bury, J. E. Mondloch, J. T. Hupp and O. K. Farha, Solvent-Assisted Linker Exchange: An Alternative to the De Novo Synthesis of Unattainable Metal–Organic Frameworks, *Angew. Chem., Int. Ed.*, 2014, **53**(18), 4530–4540.

34 P. Deria, J. E. Mondloch, E. Tylianakis, P. Ghosh, W. Bury, R. Q. Snurr, J. T. Hupp and O. K. Farha, Perfluoroalkane Functionalization of Nu-1000 Via Solvent-Assisted Ligand Incorporation: Synthesis and CO_2 Adsorption Studies, *J. Am. Chem. Soc.*, 2013, **135**(45), 16801–16804.

35 P. Deria, W. Bury, J. T. Hupp and O. K. Farha, Versatile Functionalization of the Nu-1000 Platform by Solvent-Assisted Ligand Incorporation, *Chem. Commun.*, 2014, **50**(16), 1965–1968.

36 P. Deria, Y. G. Chung, R. Q. Snurr, J. T. Hupp and O. K. Farha, Water Stabilization of Zr_6-Based Metal–Organic Frameworks Via Solvent-Assisted Ligand Incorporation, *Chem. Sci.*, 2015, **6**(9), 5172–5176.

37 R. Ifraemov, R. Shimoni, W. He, G. Peng and I. Hod, A Metal–Organic Framework Film with a Switchable Anodic and Cathodic Behaviour in a Photo-Electrochemical Cell, *J. Mater. Chem. A*, 2019, **7**(7), 3046–3053.

38 J. Yu, X. Li and P. Deria, Light-Harvesting in Porous Crystalline Compositions: Where We Stand toward Robust

Metal-Organic Frameworks, *ACS Sustainable Chem. Eng.*, 2019, **7**(2), 1841–1854.

39 B. Pattengale, S. Yang, J. Ludwig, Z. Huang, X. Zhang and J. Huang, Exceptionally Long-Lived Charge Separated State in Zeolitic Imidazolate Framework: Implication for Photocatalytic Applications, *J. Am. Chem. Soc.*, 2016, **138**(26), 8072–8075.

40 N.-N. Yang, J.-J. Fang, Q. Sui and E.-Q. Gao, Incorporating Electron-Deficient Bipyridinium Chromorphores to Make Multiresponsive Metal-Organic Frameworks, *ACS Appl. Mater. Interfaces*, 2018, **10**(3), 2735–2744.

41 Y. Zeng, Z. Fu, H. Chen, C. Liu, S. Liao and J. Dai, Photo- and Thermally Induced Coloration of a Crystalline MOF Accompanying Electron Transfer and Long-Lived Charge Separation in a Stable Host-Guest System, *Chem. Commun.*, 2012, **48**(65), 8114–8116.

42 S. Yamamoto, Y. Hijikata, Z. Zhang, K. Awaga, J. Pirillo, Y. Hijikata and K. Awaga, Nanopore-Induced Host-Guest Charge Transfer Phenomena in a Metal-Organic Framework, *Chem. Sci.*, 2018, **9**(13), 3282–3289.

43 P. Huo, T. Chen, J.-L. Hou, L. Yu, Q.-Y. Zhu and J. Dai, Ligand-to-Ligand Charge Transfer within Metal–Organic Frameworks Based on Manganese Coordination Polymers with Tetrathiafulvalene-Bicarboxylate and Bipyridine Ligands, *Inorg. Chem.*, 2016, **55**(13), 6496–6503.

44 J.-L. Wang, C. Wang and W. Lin, Metal-Organic Frameworks for Light Harvesting and Photocatalysis, *ACS Catal.*, 2012, **2**(12), 2630–2640.

45 X. Deng, J. Albero, L. Xu, H. Garcia and Z. Li, Construction of a Stable Ru-Re Hybrid System Based on Multifunctional MOF-253 for Efficient Photocatalytic CO_2 Reduction, *Inorg. Chem.*, 2018, **57**(14), 8276–8286.

46 S. Yang, D. Fan, W. Hu, B. Pattengale, C. Liu, X. Zhang and J. Huang, Elucidating Charge Separation Dynamics in a Hybrid Metal-Organic Framework Photocatalyst for Light-Driven H_2 Evolution, *J. Phys. Chem. C*, 2018, **122**(6), 3305–3311.

47 X.-J. Kong, Z. Lin, Z.-M. Zhang, T. Zhang and W. Lin, Hierarchical Integration of Photosensitizing Metal-Organic Frameworks and Nickel-Containing Polyoxometalates for Efficient Visible-Light-Driven Hydrogen Evolution, *Angew. Chem., Int. Ed.*, 2016, **55**(22), 6411–6416.

48 Y.-Z. Chen, Z. U. Wang, H. Wang, J. Lu, S.-H. Yu and H.-L. Jiang, Singlet Oxygen-Engaged Selective Photo-Oxidation over Pt Nanocrystals/Porphyrinic MOF: The Roles of Photothermal Effect and Pt Electronic State, *J. Am. Chem. Soc.*, 2017, **139**(5), 2035–2044.

49 C.-W. Kung, K. Otake, C. T. Buru, S. Goswami, Y. Cui, J. T. Hupp, A. M. Spokoyny and O. K. Farha, Increased Electrical Conductivity in a Mesoporous Metal–Organic Framework Featuring Metallacarboranes Guests, *J. Am. Chem. Soc.*, 2018, **140**(11), 3871–3875.

50 H.-Q. Xu, S. Yang, X. Ma, J. Huang and H.-L. Jiang, Unveiling Charge-Separation Dynamics in CdS/Metal–Organic Framework Composites for Enhanced Photocatalysis, *ACS Catal.*, 2018, **8**(12), 11615–11621.

51 E. A. Dolgopolova, A. M. Rice, C. R. Martin and N. B. Shustova, Photochemistry and Photophysics of Mofs: Steps Towards MOF-Based Sensing Enhancements, *Chem. Soc. Rev.*, 2018, **47**(13), 4710–4728.

52 S. Kuyuldar, D. T. Genna and C. Burda, On the Potential for Nanoscale Metal–Organic Frameworks for Energy Applications, *J. Mater. Chem. A*, 2019, **7**(38), 21545–21576.

53 S. Lin, P. M. Usov and A. J. Morris, The Role of Redox Hopping in Metal–Organic Framework Electrocatalysis, *Chem. Commun.*, 2018, **54**(51), 6965–6974.

54 W. Liu and X.-B. Yin, Metal–Organic Frameworks for Electrochemical Applications. TrAC, *Trends Anal. Chem.*, 2016, **75**, 86–96.

55 N. S. Sariciftci, L. Smilowitz, A. J. Heeger and F. Wudl, Photoinduced Electron Transfer from a Conducting Polymer to Buckminsterfullerene, *Science*, 1992, **258**(5087), 1474–1476.

56 J. Yu, W. A. Van, P. Deria, J. Park, G. Rumbles and G. Rumbles, Excited-State Electronic Properties in Zr-Based Metal-Organic Frameworks as a Function of a Topological Network, *J. Am. Chem. Soc.*, 2018, **140**(33), 10488–10496.

57 P. Deria, J. Yu, T. Smith and R. P. Balaraman, Ground-State Versus Excited-State Interchromophoric Interaction: Topology Dependent Excimer Contribution in Metal–Organic Framework Photophysics, *J. Am. Chem. Soc.*, 2017, **139**(16), 5973–5983.

58 C. A. Kent, D. Liu, L. Ma, J. M. Papanikolas, T. J. Meyer and W. Lin, Light Harvesting in Microscale Metal–Organic Frameworks by Energy Migration and Interfacial Electron Transfer Quenching, *J. Am. Chem. Soc.*, 2011, **133**(33), 12940–12943.

59 H.-J. Son, S. Jin, S. Patwardhan, S. J. Wezenberg, N. C. Jeong, M. So, C. E. Wilmer, A. A. Sarjeant, G. C. Schatz, R. Q. Snurr, O. K. Farha, G. P. Wiederrecht and J. T. Hupp, Light-Harvesting and Ultrafast Energy Migration in Porphyrin-Based Metal–Organic Frameworks, *J. Am. Chem. Soc.*, 2013, **135**(2), 862–869.

60 S. Goswami, L. Ma, A. B. F. Martinson, M. R. Wasielewski, O. K. Farha and J. T. Hupp, Toward Metal–Organic Framework-Based Solar Cells: Enhancing Directional Exciton Transport by Collapsing Three-Dimensional Film Structures, *ACS Appl. Mater. Interfaces*, 2016, **8**(45), 30863–30870.

61 R. A. Marcus and N. Sutin, Electron Transfers in Chemistry and Biology. Biochim. Biophys. Acta, *Rev. Bioenerg.*, 1985, **811**(3), 265–322.

62 M. J. Weaver, C. b. Electrochemical and H. R. Reactivity, Quantitative Comparisons of Rate Constants and Activation Parameters for Some Inorganic Outer-Sphere Reactions, *J. Phys. Chem.*, 1980, **84**(6), 568–576.

63 J.-M. Savéant and D. Tessier, Variation of the Electrochemical Transfer Coefficient with Potential, *Faraday Discuss. Chem. Soc.*, 1982, **74**(0), 57–72.

64 S. Wherland and I. Pecht, Protein-Protein Electron Transfer. A Marcus Theory Analysis of Reactions between

C Type Cytochromes and Blue Copper Proteins, *Biochemistry*, 1978, **17**(13), 2585–2591.

65 S. M. Khopde and K. I. Priyadarsini, Application of Marcus Theory of Electron Transfer for the Reactions between Hrp Compound I and II and 2,4-Disubstituted Phenols, *Biophys. Chem.*, 2000, **88**(1), 103–109.

66 L. P. Candeias, L. K. Folkes and P. Wardman, Factors Controlling the Substrate Specificity of Peroxidases: Kinetics and Thermodynamics of the Reaction of Horseradish Peroxidase Compound I with Phenols and Indole-3-Acetic Acids, *Biochemistry*, 1997, **36**(23), 7081–7085.

67 Y. Jia, T. J. DiMagno, C. K. Chan, Z. Wang, M. S. Popov, M. Du, D. K. Hanson, M. Schiffer, J. R. Norris and G. R. Fleming, Primary Charge Separation in Mutant Reaction Centers of Rhodobacter Capsulatus, *J. Phys. Chem.*, 1993, **97**(50), 13180–13191.

68 G. Renger, Mechanism of Light Induced Water Splitting in Photosystem II of Oxygen Evolving Photosynthetic Organisms, *Biochim. Biophys. Acta, Bioenerg.*, 2012, **1817**(8), 1164–1176.

69 R. A. Marcus, Chemical and Electrochemical Electron-Transfer Theory, *Annu. Rev. Phys. Chem.*, 1964, **15**(1), 155–196.

70 R. A. Marcus, Electron Transfer Reactions in Chemistry. Theory and Experiment, *Rev. Mod. Phys.*, 1993, **65**(3), 599–610.

71 S. Patwardhan and G. C. Schatz, Theoretical Investigation of Charge Transfer in Metal Organic Frameworks for Electrochemical Device Applications, *J. Phys. Chem. C*, 2015, **119**(43), 24238–24247.

72 X. Li, K. Maindan and P. Deria, Metal-Organic Frameworks-Based Electrocatalysis: Insight and Future Perspectives, *Comments Inorg. Chem.*, 2018, **38**(5), 166–209.

73 D. Rehm and A. Weller, Kinetics of Fluorescence Quenching by Electron and H-Atom Transfer, *Isr. J. Chem.*, 1970, **8**(2), 259–271.

74 W. Albert, Photoinduced Electron Transfer in Solution: Exciplex and Radical Ion Pair Formation Free Enthalpies and Their Solvent Dependence, *Z. Phys. Chem.*, 1982, **133**(1), 93–98.

75 R. Sarangi, J. Cho, W. Nam and E. I. Solomon, XAS and DFT Investigation of Mononuclear Cobalt(III) Peroxo Complexes: Electronic Control of the Geometric Structure in CoO_2 Versus NiO_2 Systems, *Inorg. Chem.*, 2011, **50**(2), 614–620.

76 S. E. Canton, X. Zhang, J. Zhang, T. B. van Driel, K. S. Kjaer, K. Haldrup, P. Chabera, T. Harlang, K. Suarez-Alcantara, Y. Liu, J. Pérez, A. Bordage, M. Pápai, G. Vankó, G. Jennings, C. A. Kurtz, M. Rovezzi, P. Glatzel, G. Smolentsev, J. Uhlig, A. O. Dohn, M. Christensen, A. Galler, W. Gawelda, C. Bressler, H. T. Lemke, K. B. Møller, M. M. Nielsen, R. Lomoth, K. Wärnmark and V. Sundström, Toward Highlighting the Ultrafast Electron Transfer Dynamics at the Optically Dark Sites of Photocatalysts, *J. Phys. Chem. Lett.*, 2013, **4**(11), 1972–1976.

77 L. Hanna, P. Kucheryavy, C. Liu, X. Zhang and J. V. Lockard, Long-Lived Photoinduced Charge Separation in a Trinuclear Iron-M_3-Oxo-Based Metal-Organic Framework, *J. Phys. Chem. C*, 2017, **121**(25), 13570–13576.

78 C. H. Hendon, D. Tiana, M. Fontecave, C. Sanchez, L. D′arras, C. Sassoye, L. Rozes, C. Mellot-Draznieks and A. Walsh, Engineering the Optical Response of the Titanium-Mil-125 Metal–Organic Framework through Ligand Functionalization, *J. Am. Chem. Soc.*, 2013, **135**(30), 10942–10945.

79 J. G. Santaclara, A. I. Olivos-Suarez, A. Gonzalez-Nelson, D. Osadchii, M. A. Nasalevich, M. A. van der Veen, F. Kapteijn, A. M. Sheveleva, S. L. Veber, M. V. Fedin, A. T. Murray, C. H. Hendon, A. Walsh and J. Gascon, Revisiting the Incorporation of Ti(IV) in UiO-Type Metal–Organic Frameworks: Metal Exchange Versus Grafting and Their Implications on Photocatalysis, *Chem. Mater.*, 2017, **29**(21), 8963–8967.

80 Y. Horiuchi, T. Toyao, M. Saito, K. Mochizuki, M. Iwata, H. Higashimura, M. Anpo and M. Matsuoka, Visible-Light-Promoted Photocatalytic Hydrogen Production by Using an Amino-Functionalized Ti(IV) Metal–Organic Framework, *J. Phys. Chem. C*, 2012, **116**(39), 20848–20853.

81 A. Santiago Portillo, H. G. Baldoví, M. T. García Fernandez, S. Navalón, P. Atienzar, B. Ferrer, M. Alvaro, H. Garcia and Z. Li, Ti as Mediator in the Photoinduced Electron Transfer of Mixed-Metal NH_2-UiO-66(Zr/Ti): Transient Absorption Spectroscopy Study and Application in Photovoltaic Cell, *J. Phys. Chem. C*, 2017, **121**, 7015–7024.

82 M. A. Nasalevich, C. H. Hendon, J. G. Santaclara, K. Svane, B. van der Linden, S. L. Veber, M. V. Fedin, A. J. Houtepen, M. A. van der Veen, F. Kapteijn, A. Walsh and J. Gascon, Electronic Origins of Photocatalytic Activity in D0 Metal Organic Frameworks, *Sci. Rep.*, 2016, **6**(1), 23676.

83 N. M. Padial, J. Castells-Gil, N. Almora-Barrios, M. Romero-Angel, I. da Silva, M. Barawi, A. García-Sánchez, V. A. de la Peña O'Shea and C. Martí-Gastaldo, Hydroxamate Titanium–Organic Frameworks and the Effect of Siderophore-Type Linkers over Their Photocatalytic Activity, *J. Am. Chem. Soc.*, 2019, **141**(33), 13124–13133.

84 J. Castells-Gil, N. M. Padial, N. Almora-Barrios, J. Albero, A. R. Ruiz-Salvador, J. González-Platas, H. García and C. Martí-Gastaldo, Chemical Engineering of Photoactivity in Heterometallic Titanium–Organic Frameworks by Metal Doping, *Angew. Chem., Int. Ed.*, 2018, **57**(28), 8453–8457.

85 S. Goswami, D. Ray, K.-i. Otake, C.-W. Kung, S. J. Garibay, T. Islamoglu, A. Atilgan, Y. Cui, C. J. Cramer, O. K. Farha, J. T. Hupp and A. Porous, Electrically Conductive Hexa-Zirconium(IV) Metal–Organic Framework, *Chem. Sci.*, 2018, **9**(19), 4477–4482.

86 D. E. Williams, E. A. Dolgopolova, D. C. Godfrey, E. D. Ermolaeva, P. J. Pellechia, A. B. Greytak, M. D. Smith, S. M. Avdoshenko, A. A. Popov and N. B. Shustova, Fulleretic Well-Defined Scaffolds: Donor–Fullerene Alignment through Metal Coordination and Its Effect on Photophysics, *Angew. Chem., Int. Ed.*, 2016, **55**(31), 9070–9074.

87 X.-P. Wu, L. Gagliardi and D. G. Truhlar, Cerium Metal–Organic Framework for Photocatalysis, *J. Am. Chem. Soc.*, 2018, **140**(25), 7904–7912.

88 P. Li, Q. Chen, T. C. Wang, N. A. Vermeulen, B. L. Mehdi, A. Dohnalkova, N. D. Browning, D. Shen, R. Anderson, D. A. Gómez-Gualdrón, F. M. Cetin, J. Jagiello, A. M. Asiri, J. F. Stoddart and O. K. Farha, Hierarchically Engineered Mesoporous Metal-Organic Frameworks toward Cell-Free Immobilized Enzyme Systems, *Chem*, 2018, **4**(5), 1022–1034.

89 J. Lyu, X. Zhang, K.-i. Otake, X. Wang, P. Li, Z. Li, Z. Chen, Y. Zhang, M. C. Wasson, Y. Yang, P. Bai, X. Guo, T. Islamoglu and O. K. Farha, Topology and Porosity Control of Metal–Organic Frameworks through Linker Functionalization, *Chem. Sci.*, 2019, **10**(4), 1186–1192.

90 Z. Chen, S. L. Hanna, L. R. Redfern, D. Alezi, T. Islamoglu and O. K. Farha, Reticular Chemistry in the Rational Synthesis of Functional Zirconium Cluster-Based Mofs, *Coord. Chem. Rev.*, 2019, **386**, 32–49.

91 S. Yuan, L. Huang, Z. Huang, D. Sun, J.-S. Qin, L. Feng, J. Li, X. Zou, T. Cagin and H.-C. Zhou, Continuous Variation of Lattice Dimensions and Pore Sizes in Metal–Organic Frameworks, *J. Am. Chem. Soc.*, 2020, **142**(10), 4732–4738.

92 C.-W. Kung, T. C. Wang, J. E. Mondloch, D. Fairen-Jimenez, D. M. Gardner, W. Bury, J. M. Klingsporn, J. C. Barnes, R. Van Duyne, J. F. Stoddart, M. R. Wasielewski, O. K. Farha and J. T. Hupp, Metal–Organic Framework Thin Films Composed of Free-Standing Acicular Nanorods Exhibiting Reversible Electrochromism, *Chem. Mater.*, 2013, **25**(24), 5012–5017.

93 P. Deria, D. A. Gómez-Gualdrón, I. Hod, R. Q. Snurr, J. T. Hupp and O. K. Farha, Framework-Topology-Dependent Catalytic Activity of Zirconium-Based (Porphinato)Zinc(II) MOFs, *J. Am. Chem. Soc.*, 2016, **138**(43), 14449–14457.

94 T. Islamoglu, S. Goswami, Z. Li, A. J. Howarth, O. K. Farha and J. T. Hupp, Postsynthetic Tuning of Metal–Organic Frameworks for Targeted Applications, *Acc. Chem. Res.*, 2017, **50**(4), 805–813.

95 A. Van Wyk, T. Smith, J. Park and P. Deria, Charge-Transfer within Zr-Based Metal-Organic Framework: The Role of Polar Node, *J. Am. Chem. Soc.*, 2018, **140**(8), 2756–2760.

96 P. J. Celis-Salazar, M. Cai, C. A. Cucinell, S. R. Ahrenholtz, C. C. Epley, P. M. Usov and A. J. Morris, Independent Quantification of Electron and Ion Diffusion in Metallocene-Doped Metal–Organic Frameworks Thin Films, *J. Am. Chem. Soc.*, 2019, **141**(30), 11947–11953.

97 K. Oisaki, Q. Li, H. Furukawa, A. U. Czaja and O. M. Yaghi, A Metal–Organic Framework with Covalently Bound Organometallic Complexes, *J. Am. Chem. Soc.*, 2010, **132**(27), 9262–9264.

98 X. Feng, Y. Song, Z. Li, M. Kaufmann, Y. Pi, J. S. Chen, Z. Xu, Z. Li, C. Wang and W. Lin, Metal–Organic Framework Stabilizes a Low-Coordinate Iridium Complex for Catalytic Methane Borylation, *J. Am. Chem. Soc.*, 2019, **141**(28), 11196–11203.

99 Y. Fang, Z. Xiao, A. Kirchon, J. Li, F. Jin, T. Togo, L. Zhang, C. Zhu and H.-C. Zhou, Bimolecular Proximity of a Ruthenium Complex and Methylene Blue within an Anionic Porous Coordination Cage for Enhancing Photocatalytic Activity, *Chem. Sci.*, 2019, **10**(12), 3529–3534.

100 J. Liu, L. R. Redfern, Y. Liao, T. Islamoglu, A. Atilgan, O. K. Farha and J. T. Hupp, Metal–Organic-Framework-Supported and -Isolated Ceria Clusters with Mixed Oxidation States, *ACS Appl. Mater. Interfaces*, 2019, **11**(51), 47822–47829.

101 H. Noh, C.-W. Kung, K.-i. Otake, A. W. Peters, Z. Li, Y. Liao, X. Gong, O. K. Farha and J. T. Hupp, Redox-Mediator-Assisted Electrocatalytic Hydrogen Evolution from Water by a Molybdenum Sulfide-Functionalized Metal–Organic Framework, *ACS Catal.*, 2018, **8**(10), 9848–9858.

102 S. Ahn, S. L. Nauert, C. T. Buru, M. Rimoldi, H. Choi, N. M. Schweitzer, J. T. Hupp, O. K. Farha and J. M. Notestein, Pushing the Limits on Metal–Organic Frameworks as a Catalyst Support: NU-1000 Supported Tungsten Catalysts for o-Xylene Isomerization and Disproportionation, *J. Am. Chem. Soc.*, 2018, **140**(27), 8535–8543.

103 H. Choi, A. W. Peters, H. Noh, L. C. Gallington, A. E. Platero-Prats, M. R. DeStefano, M. Rimoldi, S. Goswami, K. W. Chapman, O. K. Farha and J. T. Hupp, Vapor-Phase Fabrication and Condensed-Phase Application of a MOF-Node-Supported Iron Thiolate Photocatalyst for Nitrate Conversion to Ammonium, *ACS Appl. Energy Mater.*, 2019, **2**(12), 8695–8700.

104 M. B. Majewski, A. J. Howarth, P. Li, M. R. Wasielewski, J. T. Hupp and O. K. Farha, Enzyme Encapsulation in Metal–Organic Frameworks for Applications in Catalysis, *CrystEngComm*, 2017, **19**(29), 4082–4091.

105 Y. Pan, H. Li, J. Farmakes, F. Xiao, B. Chen, S. Ma and Z. Yang, How Do Enzymes Orient When Trapped on Metal–Organic Framework (MOF) Surfaces?, *J. Am. Chem. Soc.*, 2018, **140**(47), 16032–16036.

106 E. Gkaniatsou, C. Sicard, R. Ricoux, J.-P. Mahy, N. Steunou and C. Serre, Metal–Organic Frameworks: A Novel Host Platform for Enzymatic Catalysis and Detection, *Mater. Horiz.*, 2017, **4**(1), 55–63.

107 X. Li, J. Yu, D. J. Gosztola, H. C. Fry and P. Deria, Wavelength-Dependent Energy and Charge Transfer in Mof: A Step toward Artificial Porous Light-Harvesting System, *J. Am. Chem. Soc.*, 2019, **141**(42), 16849–16857.

108 J. Baek, B. Rungtaweevoranit, X. Pei, M. Park, S. C. Fakra, Y.-S. Liu, R. Matheu, S. A. Alshmimri, S. Alshehri, C. A. Trickett, G. A. Somorjai and O. M. Yaghi, Bioinspired Metal–Organic Framework Catalysts for Selective Methane Oxidation to Methanol, *J. Am. Chem. Soc.*, 2018, **140**(51), 18208–18216.

109 M. Taddei, R. J. Wakeham, A. Koutsianos, E. Andreoli and A. R. Barron, Post-Synthetic Ligand Exchange in Zirconium-Based Metal–Organic Frameworks: Beware of the Defects!, *Angew. Chem., Int. Ed.*, 2018, **57**(36), 11706–11710.

110 I. Liberman, R. Shimoni, R. Ifraemov, I. Rozenberg, C. Singh and I. Hod, Active-Site Modulation in an Fe-Porphyrin-Based Metal–Organic Framework through Ligand Axial Coordination: Accelerating Electrocatalysis and Charge-Transport Kinetics, *J. Am. Chem. Soc.*, 2020, **142**(4), 1933–1940.

111 P. Deria, W. Bury, I. Hod, C.-W. Kung, O. Karagiaridi, J. T. Hupp and O. K. Farha, Mof Functionalization Via Solvent-Assisted Ligand Incorporation: Phosphonates Vs Carboxylates, *Inorg. Chem.*, 2015, **54**(5), 2185–2192.

112 I. Hod, W. Bury, D. M. Gardner, P. Deria, V. Roznyatovskiy, M. R. Wasielewski, O. K. Farha and J. T. Hupp, Bias-Switchable Permselectivity and Redox Catalytic Activity of a Ferrocene-Functionalized, Thin-Film Metal–Organic Framework Compound, *J. Phys. Chem. Lett.*, 2015, **6**, 586–591.

113 I. Hod, O. K. Farha and J. T. Hupp, Modulating the Rate of Charge Transport in a Metal–Organic Framework Thin Film Using Host: Guest Chemistry, *Chem. Commun.*, 2016, **52**, 1705–1708.

114 S. Patwardhan and G. C. Schatz, Theoretical Investigation of Charge Transfer in Metal Organic Frameworks for Electrochemical Device Applications, *J. Phys. Chem. C*, 2015, **119**, 24238–24247.

115 C. R. McKeithan, L. Wojtas and R. W. Larsen, Guest to Framework Photoinduced Electron Transfer in a Cobalt Substituted Rwlc-2 Metal Organic Framework, *Dalton Trans.*, 2018, **47**(28), 9250–9256.

116 R. W. Larsen and L. Wojtas, Fixed Distance Photoinduced Electron Transfer between Fe and Zn Porphyrins Encapsulated within the Zn HKUST-1 Metal Organic Framework, *Dalton Trans.*, 2015, **44**(7), 2959–2963.

117 S. M. Pratik, L. Gagliardi and C. J. Cramer, Boosting Photoelectric Conductivity in Porphyrin-Based Mofs Incorporating C60, *J. Phys. Chem. C*, 2020, **124**(3), 1878–1887.

118 D. Ravelli, D. Dondi, M. Fagnoni and A. Albini, Photocatalysis. A Multi-Faceted Concept for Green Chemistry, *Chem. Soc. Rev.*, 2009, **38**(7), 1999–2011.

119 A.-N. Meng, L.-X. Chaihu, H.-H. Chen and Z.-Y. Gu, Ultrahigh Adsorption and Singlet-Oxygen Mediated Degradation for Efficient Synergetic Removal of Bisphenol a by a Stable Zirconium-Porphyrin Metal-Organic Framework, *Sci. Rep.*, 2017, **7**(1), 6297.

120 J. Park, Q. Jiang, D. Feng and H.-C. Zhou, Controlled Generation of Singlet Oxygen in Living Cells with Tunable Ratios of the Photochromic Switch in Metal–Organic Frameworks, *Angew. Chem., Int. Ed.*, 2016, **55**(25), 7188–7193.

121 A. Atilgan, T. Islamoglu, A. J. Howarth, J. T. Hupp and O. K. Farha, Detoxification of a Sulfur Mustard Simulant Using a Bodipy-Functionalized Zirconium-Based Metal–Organic Framework, *ACS Appl. Mater. Interfaces*, 2017, **9**(29), 24555–24560.

122 S. Goswami, C. E. Miller, J. L. Logsdon, C. T. Buru, Y.-L. Wu, D. N. Bowman, T. Islamoglu, A. M. Asiri, C. J. Cramer, M. R. Wasielewski, J. T. Hupp and O. K. Farha, Atomistic Approach toward Selective Photocatalytic Oxidation of a Mustard-Gas Simulant: A Case Study with Heavy-Chalcogen-Containing PCN-57 Analogues, *ACS Appl. Mater. Interfaces*, 2017, **9**(23), 19535–19540.

123 W.-H. Fang, L. Zhang and J. Zhang, A 3.6 nm Ti_{52}–Oxo Nanocluster with Precise Atomic Structure, *J. Am. Chem. Soc.*, 2016, **138**(24), 7480–7483.

124 Z.-F. Hong, S.-H. Xu, Z.-H. Yan, D.-F. Lu, X.-J. Kong, L.-S. Long and L.-S. Zheng, A Large Titanium Oxo Cluster Featuring a Well-Defined Structural Unit of Rutile, *Cryst. Growth Des.*, 2018, **18**(9), 4864–4868.

125 Y. Song, Z. Li, Y. Zhu, X. Feng, J. S. Chen, M. Kaufmann, C. Wang and W. Lin, Titanium Hydroxide Secondary Building Units in Metal-Organic Frameworks Catalyze Hydrogen Evolution under Visible Light, *J. Am. Chem. Soc.*, 2019, **141**(31), 12219–12223.

126 Z.-H. Yan, M.-H. Du, J. Liu, S. Jin, C. Wang, G.-L. Zhuang, X.-J. Kong, L.-S. Long and L.-S. Zheng, Photo-Generated Dinuclear $\{Eu(II)\}_2$ Active Sites for Selective CO_2 Reduction in a Photosensitizing Metal-Organic Framework, *Nat. Commun.*, 2018, **9**(1), 1–9.

127 J. I. Goldsmith, W. R. Hudson, M. S. Lowry, T. H. Anderson and S. Bernhard, Discovery and High-Throughput Screening of Heteroleptic Iridium Complexes for Photoinduced Hydrogen Production, *J. Am. Chem. Soc.*, 2005, **127**(20), 7502–7510.

128 D. A. Nagib, M. E. Scott and D. W. C. MacMillan, Enantioselective A-Trifluoromethylation of Aldehydes Via Photoredox Organocatalysis, *J. Am. Chem. Soc.*, 2009, **131**(31), 10875–10877.

129 A. G. Condie, J. C. González-Gómez and C. R. J. Stephenson, Visible-Light Photoredox Catalysis: Aza-Henry Reactions Via C–H Functionalization, *J. Am. Chem. Soc.*, 2010, **132**(5), 1464–1465.

130 L. Flamigni, A. Barbieri, C. Sabatini, B. Ventura and F. Barigelletti, in *Photochemistry and Photophysics of Coordination Compounds: Iridium. In Photochemistry and Photophysics of Coordination Compounds II*, ed. V. Balzani and S. Campagna, Springer Berlin Heidelberg, Berlin, Heidelberg, 2007, pp. 143–203.

131 Y. Pellegrin and F. Odobel, Sacrificial Electron Donor Reagents for Solar Fuel Production, *C. R. Chim.*, 2017, **20**(3), 283–295.

132 K. Kalyanasundaram, J. Kiwi and M. Grätzel, Hydrogen Evolution from Water by Visible Light, a Homogeneous

Three Component Test System for Redox Catalysis, *Helv. Chim. Acta*, 1978, **61**(7), 2720–2730.

133 A.-M. Manke, K. Geisel, A. Fetzer and P. Kurz, A Water-Soluble Tin(IV) Porphyrin as a Bioinspired Photosensitiser for Light-Driven Proton-Reduction, *Phys. Chem. Chem. Phys.*, 2014, **16**(24), 12029–12042.

134 G. Lan, Z. Li, S. S. Veroneau, Y.-Y. Zhu, Z. Xu, C. Wang and W. Lin, Photosensitizing Metal-Organic Layers for Efficient Sunlight-Driven Carbon Dioxide Reduction, *J. Am. Chem. Soc.*, 2018, **140**(39), 12369–12373.

135 R. N. Sampaio, D. C. Grills, D. E. Polyansky, D. J. Szalda and E. Fujita, Unexpected Roles of Triethanolamine in the Photochemical Reduction of CO_2 to Formate by Ruthenium Complexes, *J. Am. Chem. Soc.*, 2020, **142**(5), 2413–2428.

136 H. Ishida, K. Tanaka and T. Tanaka, Electrochemical CO_2 Reduction Catalyzed by Ruthenium Complexes [Ru(Bpy)2 $(CO)_2]^{2+}$ and $[Ru(Bpy)_2(CO)Cl]^+$. Effect of Ph on the Formation of Co and Hcoo, *Organometallics*, 1987, **6**(1), 181–186.

137 Y. Tamaki, T. Morimoto, K. Koike and O. Ishitani, Photocatalytic Co2 Reduction with High Turnover Frequency and Selectivity of Formic Acid Formation Using Ru(II) Multinuclear Complexes, *Proc. Natl. Acad. Sci. U. S. A.*, 2012, **109**(39), 15673–15678.

138 E. Hasegawa, S. Takizawa, T. Seida, A. Yamaguchi, N. Yamaguchi, N. Chiba, T. Takahashi, H. Ikeda and K. Akiyama, Photoinduced Electron-Transfer Systems Consisting of Electron-Donating Pyrenes or Anthracenes and Benzimidazolines for Reductive Transformation of Carbonyl Compounds, *Tetrahedron*, 2006, **62**(27), 6581–6588.

139 Z. Xia, C. He, X. Wang and C. Duan, Modifying Electron Transfer between Photoredox and Organocatalytic Units Via Framework Interpenetration for B-Carbonyl Functionalization, *Nat. Commun.*, 2017, **8**(1), 1–11.

140 I. Hod, O. K. Farha and J. T. Hupp, Modulating the Rate of Charge Transport in a Metal-Organic Framework Thin Film Using Host:Guest Chemistry, *Chem. Commun.*, 2016, **52**(8), 1705–1708.

141 K. Maindan, X. Li, J. Yu and P. Deria, Controlling Charge-Transport in Metal-Organic Frameworks: Contribution of Topological and Spin-State Variation on the Fe-Porphyrin Centered Redox Hopping Rate, *J. Phys. Chem. B*, 2019, **123**(41), 8814–8822.

142 L. Sun, M. G. Campbell and M. Dincă, Electrically Conductive Porous Metal–Organic Frameworks, *Angew. Chem., Int. Ed.*, 2016, **55**(11), 3566–3579.

143 C.-W. Kung, S. Goswami, I. Hod, T. C. Wang, J. Duan, O. K. Farha and J. T. Hupp, Charge Transport in Zirconium-Based Metal–Organic Frameworks, *Acc. Chem. Res.*, 2020, **53**(6), 1187–1195.

144 K. Natarajan, A. K. Gupta, S. N. Ansari, M. Saraf and S. M. Mobin, Mixed-Ligand-Architected 2d Co(II)-Mof Expressing a Novel Topology for an Efficient Photoanode for Water Oxidation Using Visible Light, *ACS Appl. Mater. Interfaces*, 2019, **11**(14), 13295–13303.

145 C. Zhang, X. Li, S.-z. Kang, L. Qin, G. Li and J. Mu, Photoelectronically Active, Metal Organic Framework Films Prepared by Self-Directed Assembly of Silanized Porphyrin Cobalt Monomers, *Chem. Commun.*, 2014, **50**(65), 9064–9067.

146 W. Zhang, R. Li, X. Zhao, Z. Chen, A. W.-K. Law and K. Zhou, A Cobalt-Based Metal-Organic Framework as Cocatalyst on Bivo4 Photoanode for Enhanced Photoelectrochemical Water Oxidation, *ChemSusChem*, 2018, **11**(16), 2710–2716.

147 C. A. Downes and S. C. Marinescu, Efficient Electrochemical and Photoelectrochemical H2 Production from Water by a Cobalt Dithiolene One-Dimensional Metal-Organic Surface, *J. Am. Chem. Soc.*, 2015, **137**(43), 13740–13743.

148 A. J. Bard, Photoelectrochemistry, *Science*, 1980, **207**(4427), 139–144.

149 A. Garcia-Sanchez, M. Gomez-Mendoza, M. Barawi, I. J. Villar-Garcia, M. Liras, F. Gandara and V. A. de la Pena O'Shea, Fundamental Insights into Photoelectrocatalytic Hydrogen Production with a Hole-Transport Bismuth Metal-Organic Framework, *J. Am. Chem. Soc.*, 2020, **142**(1), 318–326.

150 S. Lin, D. R. Cairnie, D. Davis, A. Chakraborty, M. Cai and A. J. Morris, Photoelectrochemical Alcohol Oxidation by Mixed-Linker Metal-Organic Frameworks, *Faraday Discuss.*, 2020, DOI: 10.1039/D0FD00021C.

151 S. Zhou, P. Yue, J. Huang, L. Wang, H. She and Q. Wang, High-Performance Photoelectrochemical Water Splitting of $BiVO_4$@Co-Mim Prepared by a Facile *in situ* Deposition Method, *Chem. Eng. J.*, 2019, **371**, 885–892.

152 B. J. C. Wong, D.-m. Xu, S.-S. Bao, L.-M. Zheng and J. Lei, Hofmann Metal-Organic Framework Monolayer Nanosheets as an Axial Coordination Platform for Biosensing, *ACS Appl. Mater. Interfaces*, 2019, **11**(13), 12986–12992.

153 M. Jurcic, W. J. Peveler, C. N. Savory, D.-K. Bucar, A. J. Kenyon, D. O. Scanlon and I. P. Parkin, Sensing and Discrimination of Explosives at Variable Concentrations with a Large-Pore Mof as Part of a Luminescent Array, *ACS Appl. Mater. Interfaces*, 2019, **11**(12), 11618–11626.

154 D. Masih, V. Chernikova, O. Shekhah, M. Eddaoudi and O. F. Mohammed, Zeolite-Like Metal-Organic Framework (Mof) Encaged Pt(II)-Porphyrin for Anion-Selective Sensing, *ACS Appl. Mater. Interfaces*, 2018, **10**(14), 11399–11405.

155 B.-X. Dong, Y.-M. Pan, W.-L. Liu and Y.-L. Teng, An Ultrastable Luminescent Metal-Organic Framework for Selective Sensing of Nitroaromatic Compounds and Nitroimidazole-Based Drug Molecules, *Cryst. Growth Des.*, 2018, **18**(1), 431–440.

156 R. Dalapati, S. Nandi, H. Reinsch, B. K. Bhunia, B. B. Mandal, N. Stock and S. Biswas, Fluorogenic Naked-Eye Sensing and Live-Cell Imaging of Cyanide by a Hydrazine-Functionalized CAU-10 Metal-Organic Framework, *CrystEngComm*, 2018, **20**(29), 4194–4201.

157 D. Ning, Q. Liu, Q. Wang, X.-M. Du, Y. Li and W.-J. Ruan, Pyrene-Based MOFs as Fluorescent Sensors for Pahs: An Energetic Pathway of the Backbone Structure Effect on Response, *Dalton Trans.*, 2019, **48**(17), 5705–5712.

158 A. Khatun, D. K. Panda, S. Saha, N. Sayresmith and M. G. Walter, Thiazolothiazole-Based Luminescent Metal-Organic Frameworks with Ligand-to-Ligand Energy Transfer and Hg(2+)-Sensing Capabilities, *Inorg. Chem.*, 2019, **58**(19), 12707–12715.

159 B. Wang, Q. Yang, C. Guo, Y. Sun, L.-H. Xie and J.-R. Li, Stable Zr(IV)-Based Metal-Organic Frameworks with Predesigned Functionalized Ligands for Highly Selective Detection of Fe(III) Ions in Water, *ACS Appl. Mater. Interfaces*, 2017, **9**(11), 10286–10295.

160 B. Yan, Lanthanide-Functionalized Metal–Organic Framework Hybrid Systems to Create Multiple Luminescent Centers for Chemical Sensing, *Acc. Chem. Res.*, 2017, **50**(11), 2789–2798.

161 Y. Cui, D. Yue, Y. Huang, J. Zhang, Z. Wang, D. Yang and G. Qian, Photo-Induced Electron Transfer in a Metal-Organic Framework: A New Approach Towards a Highly Sensitive Luminescent Probe for Fe^{3+}, *Chem. Commun.*, 2019, **55**(75), 11231–11234.

162 B. Gui, Y. Meng, Y. Xie, J. Tian, G. Yu, W. Zeng, G. Zhang, S. Gong, C. Yang, D. Zhang and C. Wang, Tuning the Photoinduced Electron Transfer in a Zr-MOF: Toward Solid-State Fluorescent Molecular Switch and Turn-on Sensor, *Adv. Mater.*, 2018, **30**(34), 1802329.

163 Q. Li, X. Wu, X. Huang, Y. Deng, N. Chen, D. Jiang, L. Zhao, Z. Lin and Y. Zhao, Tailoring the Fluorescence of Aie-Active Metal-Organic Frameworks for Aqueous Sensing of Metal Ions, *ACS Appl. Mater. Interfaces*, 2018, **10**(4), 3801–3809.

